NASA/CR–2014-218185

A Comparison of Metallic, Composite and Nanocomposite Optimal Transonic Transport Wings

Graeme J. Kennedy, Gaetan K. W. Kenway, and Joaquim R. R. Martins
University of Michigan, Ann Arbor, Michigan

March 2014

NASA STI Program . . . in Profile

Since its founding, NASA has been dedicated to the advancement of aeronautics and space science. The NASA scientific and technical information (STI) program plays a key part in helping NASA maintain this important role.

The NASA STI program operates under the auspices of the Agency Chief Information Officer. It collects, organizes, provides for archiving, and disseminates NASA's STI. The NASA STI program provides access to the NASA Aeronautics and Space Database and its public interface, the NASA Technical Report Server, thus providing one of the largest collections of aeronautical and space science STI in the world. Results are published in both non-NASA channels and by NASA in the NASA STI Report Series, which includes the following report types:

- TECHNICAL PUBLICATION. Reports of completed research or a major significant phase of research that present the results of NASA Programs and include extensive data or theoretical analysis. Includes compilations of significant scientific and technical data and information deemed to be of continuing reference value. NASA counterpart of peer-reviewed formal professional papers, but having less stringent limitations on manuscript length and extent of graphic presentations.

- TECHNICAL MEMORANDUM. Scientific and technical findings that are preliminary or of specialized interest, e.g., quick release reports, working papers, and bibliographies that contain minimal annotation. Does not contain extensive analysis.

- CONTRACTOR REPORT. Scientific and technical findings by NASA-sponsored contractors and grantees.

- CONFERENCE PUBLICATION. Collected papers from scientific and technical conferences, symposia, seminars, or other meetings sponsored or co-sponsored by NASA.

- SPECIAL PUBLICATION. Scientific, technical, or historical information from NASA programs, projects, and missions, often concerned with subjects having substantial public interest.

- TECHNICAL TRANSLATION. English-language translations of foreign scientific and technical material pertinent to NASA's mission.

Specialized services also include organizing and publishing research results, distributing specialized research announcements and feeds, providing information desk and personal search support, and enabling data exchange services.

For more information about the NASA STI program, see the following:

- Access the NASA STI program home page at *http://www.sti.nasa.gov*

- E-mail your question to help@sti.nasa.gov

- Fax your question to the NASA STI Information Desk at 443-757-5803

- Phone the NASA STI Information Desk at 443-757-5802

- Write to:
  STI Information Desk
  NASA Center for AeroSpace Information
  7115 Standard Drive
  Hanover, MD 21076-1320

NASA/CR–2014-218185

A Comparison of Metallic, Composite and Nanocomposite Optimal Transonic Transport Wings

Graeme J. Kennedy, Gaetan K. W. Kenway, and Joaquim R. R. Martins
University of Michigan, Ann Arbor, Michigan

National Aeronautics and
Space Administration

Langley Research Center
Hampton, Virginia 23681-2199

Prepared for Langley Research Center
under Cooperative Agreement NNX11AI19A

March 2014

Acknowledgments

Funding for this research was provided by NASA under grant number NNX11AI19A. The authors would like to thank Christine Jutte, Bret Stanford, and Karen Taminger for their help in defining this project and for their suggestions in the writing of this report.

Available from:

NASA Center for AeroSpace Information
7115 Standard Drive
Hanover, MD 21076-1320
443-757-5802

Contents

Abstract

Current and future composite material technologies have the potential to greatly improve the performance of large transport aircraft. However, the coupling between aerodynamics and structures makes it challenging to design optimal flexible wings, and the transonic flight regime requires high fidelity computational models. We address these challenges by solving a series of high-fidelity aerostructural optimization problems that explore the design space for the wing of a large transport aircraft. We consider three different materials: aluminum, carbon-fiber reinforced composites and an hypothetical composite based on carbon nanotubes. The design variables consist of both aerodynamic shape (including span), structural sizing, and ply angle fractions in the case of composites. Pareto fronts with respect to structural weight and fuel burn are generated. The wing performance in each case is optimized subject to stress and buckling constraints. We found that composite wings consistently resulted in lower fuel burn and lower structural weight, and that the carbon nanotube composite did not yield the increase in performance one would expect from a material with such outstanding properties. This indicates that there might be diminishing returns when it comes to the application of advanced materials to wing design, requiring further investigation.

1 Introduction

The goal of NASA's high aspect ratio wing work under the Fixed Wing project is to explore ways to increase wing span and thus reduce induced drag without an excessive increase in structural weight. The exploration of the wing design space requires the consideration of both aerodynamics and structures due to wing flexibility and the inherent trade-offs between drag and structural weight in the design. This is especially important in the high aspect ratio wings considered in this study, since wings become more flexible as span is increased. In this report we explore the use of three different materials: aluminum, carbon-fiber reinforced composites and an hypothetical composite based on carbon nanotubes.

In the following sections, we describe a series of structural and aerostructural design problems that we solved. The objective of this sequence of design problems is to evaluate the impact of new structural material technologies on the trade-offs in the design of a conventional aircraft wing. In order to perform this assessment, we use a series of structural and coupled aerostructural optimization problems that are described in detail below. Optimization of each candidate design is necessary to make a fair comparison between potential technologies, so that the full benefit of the potential technology is realized. Comparing sub-optimal designs may lead to incorrect conclusions regarding the relative merits of different technologies. However, the design optimization problem must also adequately capture the requirements and objective of a realistic aircraft design problem, otherwise the predicted performance improvements may be a result of an incomplete analysis or an inadequate design.

The remainder of this document is structured as follows: in Section 2 we describe the essential aspects of the analysis and design tools used for this study. In Section 3 we present the geometry we use in this study. In Section 4 we describe a series of structural design parametrizations used in the following studies. In Section 5 we present the aerostructural design problem formulation. In Section 6 we present some results and in the last section we present conclusions and future work for the project.

2 Analysis tools

In the studies performed for this project, all the functions of interest in the design problem, such as objectives or constraints, are evaluated at converged aerostructural solutions. In this report we use the term *aerostructural analysis* to refer to the static aeroelastic analysis of an aircraft such that the aerodynamic forces on the deformed flying shape of the aircraft are in equilibrium with the inertial forces. In this study, aerostructural analysis is necessary due to the flexibility of the designs obtained using advanced materials. As a result, it is necessary to fully capture the aerostructural effects within the design space to fully model the performance of the aircraft. Since gradient-based design optimization often requires several hundred gradient and function evaluations, an efficient aerostructural solution and gradient evaluation technique is required. In this work, we use both a medium fidelity method that uses a panel method, with compressibility, viscous and wave drag corrections coupled to a high-fidelity finite-element solver, and a CFD solver that can solve either the Euler or RANS equations coupled to the same finite-element solver. Due to the large dimensionality of the design space and the computational cost of the analysis, we exclusively use adjoint-based gradient evaluation techniques [1, 2]. The following section outlines the aerostructural analysis and adjoint-based gradient evaluation techniques used within this work. Additional details about the

solution methods and the efficiency of the approach can be found in Kennedy and Martins [3] and Kenway *et al.* [4].

2.1 Aerodynamic analysis

For the medium-fidelity aerostructural cases, the aerodynamic analysis is performed using TriPan, an unstructured, three-dimensional parallel panel code for calculating the aerodynamic forces, moments and pressures for inviscid, incompressible, external lifting flows using the Prandtl–Glauert equation [3]. TriPan uses constant first-order source and doublet singularity elements distributed over the entire lifting surface and doublet elements distributed over the wake [5]. The source strengths are determined based on the onset flow conditions while the boundary conditions for the doublet strengths constitute a dense linear system of equations, represented here by

$$\mathbf{R}_A(\mathbf{w}, \mathbf{u}) = 0, \tag{1}$$

where $\mathbf{u}$ and $\mathbf{w}$ are vectors of the structural and aerodynamic state variables, respectively. The linear system represented by Equation (1) is solved in parallel using PETSc [6]. A dense matrix format is used for the matrix-vector products, while a sparse approximate-Jacobian is used to form a incomplete LU (ILU) preconditioner. The linear system is solved using the Krylov subspace method GMRES.

For the high-fidelity aerodynamic cases, we use the CFD solver SUmb, which is a second-order structured block-based finite-volume solver for the Euler, Navier–Stokes and RANS equations. SUmb has both a multi-grid solution method with an explicit Runge–Kutta time integration method with residual smoothing, and an inexact Newton–Krylov solution method with a non-monotone linesearch strategy. For the Newton–Krylov method, the linear systems arising at each Newton step are solved using the Krylov subspace methods with the parallel algorithms available in PETSc [6]. Typically, the multi-grid scheme is used during the start-up phase, while the Newton–Krylov method is employed once the relative residual norm is reduced below a target tolerance. The combination of these two methods provides a fast and robust solution strategy that can handle significant design modifications during an optimization. Kenway *et al.* [4, 7] describe further details of the most important aspects of the solver.

2.1.1 Drag build up

When using TriPan it is essential that the aerodynamic effects not captured by linear potential methods be modeled as accurately as possible, so that the drag calculations provide reasonably accurate estimates of the total aircraft drag. Here, we outline the drag build-up calculations performed in this study. The drag build-up consists of the induced drag, computed directly from TriPan using a Trefftz-plane integration, with additional empirical drag corrections including a surface friction correction, profile drag corrections and drag-divergence.

The profile drag is computed based on a quadratic model of the sectional drag coefficient:

$$c_{d_p} = c_{d0} + c_{d2} c_l^2, \tag{2}$$

where c_{d_p} is the profile drag, c_l is the sectional lift coefficient, and c_{d0} and c_{d2} are coefficients defined below. The coefficient c_{d0} is based on the skin friction estimate

$$c_{d0} = F_c c_f,$$

where F_c is a profile drag form-factor, and c_f is the turbulent skin-friction coefficient determined using the van Driest II method [8]. The form-factor, F_c, is computed using the thickness to chord ratio, t/c, as follows:

$$F_c = 1 + 2.7\left(\frac{t}{c}\right) + 100\left(\frac{t}{c}\right)^4.$$

Finally, based on the method presented by Wakayama and Kroo [9], the quadratic coefficient in Equation (2), is computed based on the expression:

$$c_{d2} = \frac{0.38}{\cos^2\Lambda} c_{d0},$$

where Λ is the leading-edge sweep angle.

The compressibility drag is computed based on a crest-critical Mach number computed using the Korn equation,

$$M_{\text{crit}} = \frac{\kappa_A}{\cos\Lambda} - \frac{t/c}{\cos^2\Lambda} - \frac{c_l}{10\cos^3\Lambda} - \left(\frac{0.1}{80}\right)^{1/3}, \tag{3}$$

where κ_A is a technology factor that we set to $\kappa_A = 0.95$, which is suitable for supercritical airfoil sections commonly used in transport aircraft. The sectional contribution to the compressibility drag is then computed using

$$c_{d_c} = 20(M - M_{\text{crit}})^4 \tag{4}$$

for $M > M_{\text{crit}}$.

2.2 Load transfer

The load and displacement transfer scheme follows the work of Brown [10]. The displacements from the structures are extrapolated to the aerodynamic nodes using rigid links. These rigid links are formed by locating the closest point on the structural surface to each of the aerodynamic nodes. The structural surface is determined by interpolating between structural nodes using the finite-element shape functions. The displacements $\mathbf{u}_S$ and rotations $\boldsymbol{\theta}_S$ on the structural surface, and the rigid links $\mathbf{r}$ are used to determine the displacements of the aerodynamic nodes $\mathbf{u}_A$ as follows:

$$\mathbf{u}_A = \mathbf{u}_S + \boldsymbol{\theta}_S \times \mathbf{r}. \tag{5}$$

Note that this formula uses a small angle approximation. Equation (5) can be used, in conjunction with the method of virtual work, to form the consistent force vector for the aerodynamic forces at the structural nodes. More details of the approach are outlined in Kennedy and Martins [3].

2.3 Structural analysis

The structural analysis is performed using the Toolkit for the Analysis of Composite Structures (TACS), a parallel, finite-element code designed specifically for the analysis of stiffened, thin-walled, composite structures using either linear or geometrically nonlinear strain relationships [3]. In the work to date, we have exclusively used linear structural analysis, however, geometrically nonlinear analysis may be required to accurately predict the flying shape of very flexible aircraft. In addition, we have focused on using a smeared stiffness approach in which the effect of stiffeners are included in the stiffness of the skin as described in detail below, as a result, we have not used the full stiffened

shell analysis capabilities of TACS. When modeling stiffened shell structures, we typically use third order finite-element discretizations that provide a good trade-off between solution accuracy and gradient-evaluation costs.

The residuals of the structural governing equations are

$$\mathbf{R}_S(\mathbf{w}, \mathbf{u}) = \mathbf{S}_c(\mathbf{u}) - \mathbf{F}(\mathbf{w}, \mathbf{u}), \tag{6}$$

where $\mathbf{u}$ is a vector of displacements and rotations, $\mathbf{S}_c$ are the residuals due to conservative forces and internal strain energy and $\mathbf{F}$ are the follower forces due to aerodynamic loads.

The Jacobian of the structural residuals involves two terms: the stiffness, or tangent stiffness matrix $\mathbf{K} = \partial \mathbf{S}_c / \partial \mathbf{u}$ and the derivative of the consistent force vector with respect to the structural displacements. This results in the following expression for the Jacobian of the structural residuals:

$$\frac{\partial \mathbf{R}_S}{\partial \mathbf{u}} = \mathbf{K} - \frac{\partial \mathbf{F}}{\partial \mathbf{u}}. \tag{7}$$

While the matrices involved in structural problems are typically symmetric, the term $\partial \mathbf{F} / \partial \mathbf{u}$ is non-symmetric due to the non-conservative nature of the aerodynamic forces. These non-symmetric matrices require different solution algorithms than those typically employed in structural finite-element codes. We use GMRES [11] to solve the non-symmetric, linear systems involving the matrix in Equation (7).

2.4 Approximate Newton–Krylov method

The aerostructural residuals are the concatenation of the aerodynamic and structural residuals, represented by:

$$\mathbf{R}(\mathbf{q}, \mathbf{x}) = \begin{bmatrix} \mathbf{R}_A(\mathbf{w}, \mathbf{u}, \mathbf{x}) \\ \mathbf{R}_S(\mathbf{w}, \mathbf{u}, \mathbf{x}) \end{bmatrix} = 0, \tag{8}$$

where $\mathbf{R}_A$ and $\mathbf{R}_S$ are the aerodynamic and structural residuals, $\mathbf{w}$ and $\mathbf{u}$ are the aerodynamic and structural state variables, $\mathbf{q}$ is the full set of aerostructural state variables $\mathbf{q}^T = [\mathbf{w}^T, \mathbf{u}^T]$, and $\mathbf{x}$ is a vector of design variables.

Newton's method applied to Equation (8) results in the following linear system of equations for the update $\Delta \mathbf{q}^{(n)}$,

$$\frac{\partial \mathbf{R}}{\partial \mathbf{q}} \Delta \mathbf{q}^{(n)} = -\mathbf{R}(\mathbf{q}^{(n)}), \tag{9}$$

where the n^{th} update is applied as follows: $\mathbf{q}^{(n+1)} = \mathbf{q}^{(n)} = \Delta \mathbf{q}^{(n)}$. In our Newton–Krylov approach, we solve an approximate linearization of the system (9) inexactly, to a loose tolerance, using a Krylov subspace method. Additionally, we use an approximate linearization that is less expensive to compute than the exact Jacobian, leading to better overall solution performance. We form a precondition for the Krylov subspace method based on discipline-level preconditioners by dropping the off-diagonal coupling terms. Note that these coupling terms are retained for the matrix-vector products which are computed using a product-rule implementation that is discussed in further detail in Kennedy and Martins [3].

2.5 Adjoint-based gradient computation

Efficient gradient-based optimization requires the accurate and efficient evaluation of gradients of the objective function and constraints. In the aerostructural optimization problem described below, there are typically far fewer objective and constraint functions than there are design variables. While there are various sensitivity methods that can be used to compute accurate derivatives [12], the coupled adjoint method [13, 14], is the most computationally efficient for coupled systems when the gradients of a small number of functions of interest are required with respect to many design variables. We have developed a coupled aerostructural adjoint that is based entirely on analytic derivatives without the use of finite-difference computations. Further details of this approach are presented in Kennedy and Martins [3]. The aerostructural adjoint equations can be written in the following form:

$$\frac{\partial \mathbf{R}}{\partial \mathbf{q}}^T \boldsymbol{\psi} = \frac{\partial f}{\partial \mathbf{q}}^T, \tag{10}$$

where $\boldsymbol{\psi}$ is the adjoint vector and $f(\mathbf{q}, \mathbf{x})$ is either an aerodynamic or structural function of interest. Once the adjoint vector has been determined using Equation (10), the total derivative is determined using the additional computation:

$$\nabla_{\mathbf{x}} f = \frac{\partial f}{\partial \mathbf{x}} - \boldsymbol{\psi}^T \frac{\partial \mathbf{R}}{\partial \mathbf{x}}. \tag{11}$$

We use a Krylov method to solve the linear coupled aerostructural adjoint equations (10) in an analogous manner to the Krylov method applied to the linearized Newton system. In the Krylov approach, the matrix-vector products are computed using the exact Jacobian-transpose of the coupled aerostructural system. One iteration of a transpose block Jacobi iteration is used as the preconditioner.

3 The QCRM wing

For this study we have developed what we call the Quasi-CRM (QCRM) geometry. The QCRM is a wing and wing-tail geometry that has a planform roughly the same as the Common Research Model (CRM) used in the DPW 4 and 5 workshops [15]. However, it should be emphasized that the QCRM geometry is not derived from the CRM geometry directly.

The QCRM wing is shown in Figure 1. The QCRM wing is untwisted, has a root chord of 12 m, a tip chord of 2.75 m, a semi-span of 30 m and a quarter-chord sweep of 35°. The leading edge of the wing is straight, while the trailing edge of the wing is quadratically interpolated between the root trailing edge and the tip. The trailing edge is determined using a quadratic spline where a control point is added at a span-wise location of 10.5 m, with a chord of 6.5 m. The curved trailing edge corresponds roughly with a wing crank, but is entirely smooth. The wing is constructed using a set of lofted super-critical NASA SC(2)-0414 and SC(2)-0610 airfoil sections. While the initial aerodynamic performance of this wing is poor, we do not use its initial performance as a baseline. Instead, we only compare optimized designs.

The QCRM geometry has several advantages over the CRM for parametric design studies. The QCRM is based on the jig shape of the wing and does not implicitly assume any aeroelastic deflection, as in the case of the CRM geometry. This greatly simplifies aerostructural design studies since the wing deflections do not have to be removed from the wing geometry. In addition,

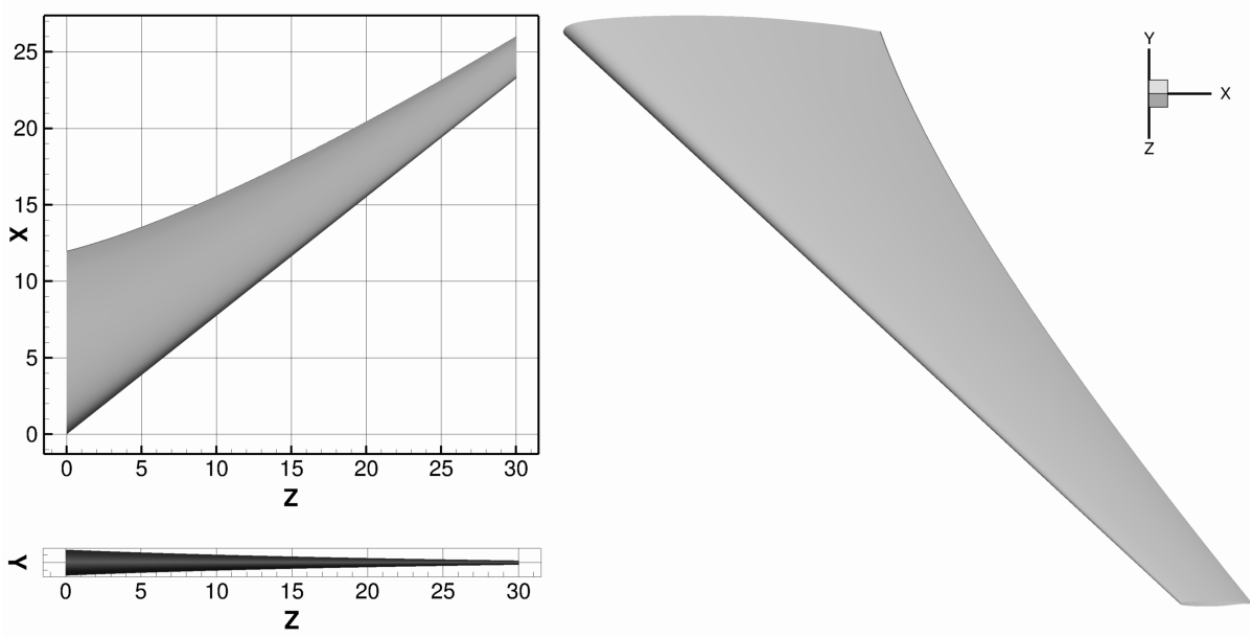

Figure 1: The Quasi-CRM (QCRM) wing geometry.

the QCRM geometry has a simple parametric description, and as a result, the wing planform can easily be manipulated using a small number of geometric design variables. Since the QCRM wing is untwisted, the aerodynamic performance of the wing will be poor, however, we always compare the performance of optimized designs so the initial planform and twist distributions are unimportant.

The internal wing structure geometry is shown in Figure 2. The wing box structure consists of two structural spars and 44 ribs as well as top and bottom wing skins. In addition, non-structural elements are added to the model to improve the load and displacement transfer between the aerodynamic and structural models. These non-structural elements consist of the leading edge skin and a false trailing edge spar and skin that extend behind the true trailing edge spar. A more detailed wing model could include the control surfaces and leading and trailing edge support structures. However, fully modeling these additional features is not considered here due to the additional complexity. Furthermore, it would be necessary to add additional load cases to the design problem to properly size these portions of the structure, complicating the design problem formulation. We have also experimented with the complete omission of the leading and trailing edge surfaces, but this leads to difficulties, as the structural displacements must be extrapolated to the aerodynamic surface. When the structural and aerodynamic surfaces are far apart, the extrapolation of the deformed aerodynamic surface becomes inaccurate and maintaining a smooth deformed surface can be difficult. As a result, we include these non-structural elements as a compromise. One of the primary purposes of the structural model is to provide an accurate weight estimate based on the primary structure within the wing. Therefore, we omit the non-structural components from the weight estimate and set them with a minimum thickness determined by the part type, which is described in more detail below. Furthermore, we reduce the stiffness of these components and maintain a consistent Poisson's ratio to avoid stress concentration effects.

Within the wing box, the first 3 ribs in the structure are parallel to the symmetry plane. This section of the wing box lies within the fuselage and is designed to model the center wing-box.

Figure 2: The QRM structural wing box

The leading and trailing edge spars lie at 15% and 65% of the root chord, respectively, while the non-structural trailing edge extends all the way to 90% of the chord.

We have used two structural finite-element models of the structure. The smaller model consists of 39 134 second order MITC4 shell finite-elements with 36 417 nodes, and roughly 218 500 degrees of freedom. The larger model is obtained by refining each second order element within the first model to obtain a third order MITC9 shell element. This larger model consists of 39 134 third order MITC9 shell finite-elements with 75 551 nodes and roughly 453 000 degrees of freedom.

4 Structural design parametrizations

In this section, we describe in detail the three structural parametrizations that we implemented. These are presented in increasing degree of complexity.

4.1 SP1: Basic metallic sizing

In this structural parametrization we assign a structural thickness variable to all structural components within the structural model. The thickness variable is treated as the thickness of an unstiffened component of the structure. This parametrization produces structural designs that are heavier than a structure with stiffened construction since the unstiffened panels exhibit low stiffness-to-weight ratios, particularly under bending loads.

In addition to structural failure constraints, which we discuss in detail below, we also impose constraints on the change in thicknesses between adjacent structural components. For instance, within the wing skin we limit both the span-wise and chord-wise change in thickness between adjacent panels. These constraints are designed to address both manufacturing requirements and un-modeled structural effects from out-of-plane shear. These adjacency constraints can be expressed as follows:

$$-\Delta \leq x_i - x_j \leq \Delta \qquad (i,j) \in \mathcal{A} \tag{12}$$

which is equivalent to imposing $|x_i - x_j| \leq \Delta$. Here $\mathcal{A}$ is a set of paired indices as follows:

$$\mathcal{A} = \{(i_1, j_1), (i_2, j_2), \ldots, (i_n, j_n)\},$$

such that an adjacency constraint is imposed between design variables x_{i_k} and x_{j_k} for $k = 1, \ldots, n$. In this case, we impose the adjacency constraint (12) to control how quickly the skin and spar thickness may change along the wing.

4.2 SP2 and SP3: Metallic, composite and CNT-based composite sizing with smeared stiffness

The issue with the structural parametrization SP1 is that each panel is treated as an unstiffened shell. As a result, the structural components exhibit lower stiffness and strength-to-weight ratios than an equivalent stiffened panel manufactured using the same technology. In order to include the effect of stiffeners, we use a smeared stiffness approach, which avoids the more onerous modeling requirements for discrete stiffeners, but has better predictive capability than the SP1 parametrization described above. We label these parametrizations SP2 and SP3 for the metallic and composite smeared stiffness parametrizations, respectively. In addition, we model a Carbon-nanotube-based composite with hypothetical properties using the SP3 parametrization as well. In the smeared stiffener approach the effect of the stiffeners on the stiffness of the panels is included in the material properties of the panel directly rather than modeling each discrete stiffener individually. This approach works reasonably well when the ratio of the panel side-length to stiffener pitch is high, meaning that there is a high density of stiffeners [16].

In the parametrizations SP2 and SP3, we split the wing structure into approximately flat panels that are analyzed and designed based on the stress state in global finite-element model under a series of loading conditions. These panels consist of the structural components formed between the ribs and spars. In order to obtain an accurate estimate of the overall wing-box weight it is necessary to have a design tool that can correctly size panels over a wide range of loading conditions. The panels range from relatively lightly loaded at the tip to heavily loaded at the wing root. Over this range, it is most important to capture the behavior of the heavily loaded parts of the structure, since these structural components will have the greatest impact on the structural wing weight.

In the present work, we have developed a design tool that predicts the stiffness of the panel based on a smeared-stiffener approach. This tool can also be used to enforce strength, buckling, and manufacturing constraints, as well as adjacency constraints that impose limits on the variation of the design variables between adjacent panels. The sizing of the panel is based on the simplified stiffness calculations and buckling criteria proposed by Stroud and Agranoff [16].

In order to avoid some of the more challenging aspects of composite design problems, we do not design the exact stacking sequence of the structure. Instead, we obtain an approximate design based on the fractions of plies at given angles. Here, we restrict the possible ply angles to 0^o, $\pm 45^o$ and 90^o, where we enforce a balanced laminate by requiring that the ply fractions of the positive and negative 45^o plies are equal. The in-plane strength and stiffness can be determined exactly using the ply fraction variables alone [17], however, the bending stiffness, bending strength, and buckling characteristics of the laminate cannot be determined exactly without knowledge of the laminate stacking sequence. Instead we use conservative estimates of the exact quantities, where possible. Most importantly, these formula approach the exact formula for very thick panels.

4.2.1 Smeared panel stiffness calculations

The ply fractions of the skin-panel are denoted $f_i^{(p)}$, while the ply fractions in the stiffener are denoted $f_i^{(s)}$. The stiffness of the panel and stiffener are based on a stiffness weighted by the ply

fractions:

$$\mathbf{Q}^{(p)} = \sum_{i=1}^{4} f_i^{(p)} \bar{\mathbf{Q}}(\theta_i), \qquad \mathbf{Q}^{(s)} = \sum_{i=1}^{4} f_i^{(s)} \bar{\mathbf{Q}}(\theta_i),$$

where $\theta_i = \{-45^o, 0^o, 45^o, 90^o\}$, $\bar{\mathbf{Q}}(\theta)$ is the stiffness in the global axis, and $\mathbf{Q}^{(p)}$ and $\mathbf{Q}^{(s)}$ are the weighted stiffness of the skin and stiffener, respectively. Note, that ply fractions are not independent, and must satisfy the following linear constraints:

$$\sum_{i=1}^{4} f_i^{(p)} = 1, \qquad \sum_{i=1}^{4} f_i^{(s)} = 1.$$

The stiffness of the overall panel is determined by accounting for the effect of the discrete stiffeners by adding additional bending and shear stiffness to the skin stiffness. The panel stiffness can be determined based on the panel thickness t_p, the stiffener height h_s, the stiffener width t_w, the stiffener pitch s_p, and the stiffness of the skin and stiffener $\mathbf{Q}^{(p)}$ and $\mathbf{Q}^{(s)}$. The smeared panel stiffness matrices are written as follows:

$$\begin{aligned} \mathbf{A} &= t_p \mathbf{Q}^{(p)} + \mathbf{A}^{(s)}, \qquad \mathbf{B} = \mathbf{B}^{(s)}, \\ \mathbf{D} &= \frac{t_p^3}{12} \mathbf{Q}^{(p)} + \mathbf{D}^{(s)}, \quad \mathbf{A}_s = \mathbf{A}_s^{(p)} + \mathbf{A}_s^{(s)}. \end{aligned} \tag{13}$$

The non-zero components of the matrices $\mathbf{A}^{(s)}$, $\mathbf{B}^{(s)}$, $\mathbf{D}^{(s)}$, and $\mathbf{A}_s^{(s)}$ are:

$$\begin{aligned} \mathbf{A}_{11}^{(s)} &= \frac{E_s A_s}{s_p}, & \mathbf{B}_{11}^{(s)} &= -\frac{h_s}{2s_p} E_s A_s, \\ \mathbf{D}_{11}^{(s)} &= \frac{E_s (h_s^2 A_s + 4I_s)}{4s_p}, & \mathbf{A}_s^{(s)}{}_{11} &= \frac{5G_s A_s}{6s_p}, \end{aligned}$$

where, $E_s = Q_{11}^s - \dfrac{Q_{21}^s Q_{12}^s}{Q_{66}^s}$ is the extension modulus of the stiffener, A_s is the area of the stiffener, and I_s is the second moment of area of the stiffener.

4.2.2 Panel-level failure analysis

Each panel in the structure must be constrained such that the response under each loading condition lies within an allowable operational envelope. In this study, we impose this envelope by considering both failure constraints and buckling constraints. For the metallic cases, the failure envelope is modeled using a von Mises stress failure criterion, while for the composite and CNT-based composite cases, the failure envelope is calculated based on a maximum strain failure criterion. This maximum strain failure criterion can be written as follows:

$$\max \left\{ \frac{\epsilon_1}{\epsilon_{1_t}}, \frac{\epsilon_1}{\epsilon_{1_c}}, \frac{\epsilon_2}{\epsilon_{2_t}}, \frac{\epsilon_2}{\epsilon_{2_c}} \frac{\gamma_{12}}{\gamma_{12_s}}, -\frac{\gamma_{12}}{\gamma_{12_s}} \right\} \tag{14}$$

where ϵ_1, ϵ_2 and γ_{12} are the normal, transverse and engineering shear strains in the local ply axis. The constants ϵ_{1_t}, ϵ_{1_c} are the maximum allowable tensile and compressive strains along the fiber direction, while ϵ_{2_t} and ϵ_{2_c} are the maximum tensile and compressive strains in the transverse directions, and γ_{12_s} is the maximum in-plane shear strain allowable. This failure criteria is applied at all ply angles for the outer-most fibers in the skin, and the lowest fiber in the stiffener. This results in 12 separate failure criteria for each point in the panel where the failure constraint is applied.

	Overall buckling	Skin buckling
$N_{1,cr}$	$\dfrac{\pi^2 EI_s}{s_p L_x^2}$	$\dfrac{2\pi^2}{s_p^2}\left(\sqrt{D_{11}D_{22}} + D_{12} + 2D_{66}\right)$
$EI_s = z_n^2(t_p s_p E_p + t_s h_s f_b E_s) + E_s\left(t_s\dfrac{h_s^3}{12} + t_s h_s\left(z_n - \dfrac{h_s}{2}\right)^2\right)$		
$z_n = \dfrac{C_n}{A_n}$	$C_n = E_s\dfrac{h_s^2}{2}t_s$	$A_n = E_p s_p t_p + E_s h_s t_s(1+f_b)$
$N_{12,cr}$	$\xi = \dfrac{\sqrt{D_1 D_2}}{D_3}$	$\xi = \dfrac{\sqrt{D_{11}D_{22}}}{D_{12}+2D_{66}}$
If $\xi > 1$	$\dfrac{4}{L_x^2}(D_1^3 D_2)^{0.25}\left(8.125 + \dfrac{5.045}{\xi}\right)$	$\dfrac{4}{s_p^2}(D_{11}D_{22}^3)^{0.25}\left(8.125 + \dfrac{5.045}{\xi}\right)$
If $\xi \leq 1$	$\dfrac{4}{L_x^2}\sqrt{D_1 D_3}(11.7 + 0.532\xi + 0.938\xi^2)$	$\dfrac{4}{s_p^2}\sqrt{D_{22}(D_{12}+2D_{66})}(11.7 + 0.532\xi + 0.938\xi^2)$

Table 1: A summary of the critical load computations for the overall and skin buckling constraints. Note that A_n and C_n are the modulus-weighted zeroth and first moments of area of the panel and stiffener, and z_n is the modulus-weighted centroid. The bending stiffness EI_s can then be used to determine the critical buckling load.

4.2.3 Panel-level buckling analysis

The buckling constraints are imposed by constraining several independent buckling modes including buckling of the skin between stiffeners, buckling of the stiffeners, and overall panel buckling including stiffeners and skins. The overall critical buckling loads are determined based on the approach of Stroud and Agranoff [16]. The skin and stiffener buckling loads are determined by assuming that the panel ends are simply supported along the lines of attachment with adjacent structural components. The critical loads are determined under the assumption that the panels are nearly flat, and therefore the analysis ignores any curvature effects.

We assume that the interaction between the longitudinal and shear buckling modes collapses into the following buckling envelope:

$$B(N_1, N_{12}) = \frac{N_{12}^2}{N_{12,cr}^2} + \frac{N_1}{N_{1,cr}} \leq 1, \tag{15}$$

where N_1 and N_{12} are the longitudinal and shear loads respectively and $N_{1,cr}$ and $N_{12,cr}$ are the critical longitudinal and shear buckling loads. Note that N_1 and N_{12} are computed in a locally aligned panel axis. Equation (15) is applied separately to the overall panel buckling, stiffener buckling and inter-stiffener skin buckling. The critical loads, $N_{1,cr}$ and $N_{12,cr}$ are determined based on the formula presented in Table 1.

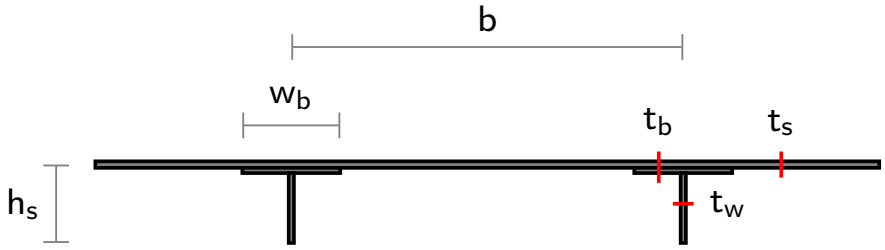

Figure 3: The panel geometry and thickness design variables used in the structural design parametrization.

5 Aerostructural design formulation

In this section, we describe the aerostructural design problem formulation and present the results of a study comparing wings with different structural technologies. In the aerostructural design problem, we have tried to develop a representative aircraft design problem formulation that captures the most essential aspects of the aircraft design problem in order to capture the tradeoff between aerodynamic performance and structural weight reduction. This is essential in order to make a fair comparison between potential benefits of candidate structural technologies.

In this design formulation, we minimize a weighted combination of fuel burn and take-off gross weight (TOGW) over a series of prescribed missions. The contribution to the objective from each mission is weighted based on the proportion of flights flown for each distance. As a result, frequently flown missions have a larger impact on the objective, while less frequently used missions have a smaller impact. We compute the fuel consumption for each mission based on the Breguet range equation as follows:

$$\mathrm{FB} = \mathrm{LGW}\left(\exp\left(\frac{R\,\mathrm{TSFC}}{V\ (L/D)}\right) - 1\right), \tag{16}$$

where FB is the fuel burn for the entire mission, LGW is the landing gross weight, R is the mission range, TSFC is the thrust-specific fuel consumption, V is the cruise speed and L/D is the lift to drag ratio. The issue with this equation, however, is that the L/D must be evaluated at some point in the mission. However, due to aerostructural effects, the deformed, flying shape of the wing, and thus L/D, will vary over the mission due primarily to changes in the aircraft weight, even at fixed C_L. A more accurate analysis would integrate the true aircraft L/D over the mission profile using the Breguet range integral. We leave this refinement for future work.

The contribution to the objective function for each mission is a weighted combination of fuel burn and takeoff gross-weight, written as follows:

$$\begin{aligned} f_i(\mathbf{x}) &= \beta \mathrm{FB}_i + (1-\beta)\mathrm{TOGW}_i \\ &= \beta \mathrm{FB}_i + (1-\beta)(\mathrm{LGW}_i + \mathrm{FB}_i) \\ &= \mathrm{FB}_i + (1-\beta)\mathrm{LGW}_i \\ &= \mathrm{LGW}_i\left(\exp\left(\frac{R_i\,\mathrm{TSFC}_i}{V_i\ (L/D)_i}\right) - \beta\right) \end{aligned} \tag{17}$$

Parameter	Value
Initial O.E.W.	138 100 kg
Fixed O.E.W. (no wing structure)	108 100 kg
Max payload	55 000 kg
span	60 m
root chord	13 m
S_{ref}	430 m^2

Table 2: Parameters used for the aircraft design problem.

where we have used the fact that TOGW = LGW+FB. Here, $f_i(\mathbf{x})$ is the un-weighted contribution to the objective from the i-th mission. Finally, the design objective can be written as follows:

$$f(\mathbf{x}) = \sum_i^N w_i f_i(\mathbf{x}) = \sum_i^N w_i \text{LGW}_i \left(\exp\left(\frac{R_i \, \text{TSFC}_i}{V_i \, (L/D)_i} \right) - \beta \right), \tag{18}$$

where w_i are the weights associated with each mission. Here we select weights such that:

$$\sum_i^N w_i = 1 \tag{19}$$

however, any scalar multiple of these weights will yield the same design.

5.1 Mission parameters

In this section, we describe in detail the parameters that are used in the mission analysis. These aircraft parameters are based roughly on a next-generation 777-sized aircraft. Table 2 shows the parameters used in the aircraft design problem. Here we estimate the overall aircraft weight based on a fixed operational empty weight (OEW) plus a variable OEW contribution that corresponds to the wing structure. The fixed portion of the OEW is 108 100 kg based on the 777-200ER with a 30 000 kg wing weight estimated as 10% of MTOW.

The weight of the aircraft at any point in flight is the sum of the fixed portion of OEW, the structural wing weight, a wing-area dependent weight factor, the payload weight and the fuel weight. In addition, the fuel weight is broken up into mission fuel and reserve fuel. The reserve fuel is calculated based on a 45 minute loiter at sub-optimal L/D and TSFC conditions, and a diversion to the furthest alternate airport for which we use a constant 500 nautical mile mission. For ease of presentation, we fix the reserve fuel at 14 100 kg throughout the design. For all missions considered here, we evaluate the L/D performance of the aircraft at the point in the mission where half of the mission fuel has been consumed.

In this study, we utilize the four missions outlined in Table 3. These are shown within a payload-range diagram in Figure 4. We analyze the performance of the aircraft at two extreme points on the payload-range diagram: the maximum range mission at the maximum payload weight and the maximum range mission at maximum fuel capacity. The maximum payload is set at 55 000 kg for this aircraft, based on the 777-200ER. Furthermore, we fix the payload of the maximum range mission at maximum fuel capacity to 15 000 kg for a 9000 nautical mile mission.

Mission 1: Max payload at maximum range			
payload	55 000 kg	range	6000 nm
w_1	0.1	L/D altitude	33 000 ft
M	0.85		
Mission 2: Max range at max fuel capacity			
payload	15 000 kg	range	9000 nm
w_2	0.1	L/D altitude	34 000 ft
M	0.85		
Mission 3: New York to London			
payload	30 000 kg	range	3040 nm
w_3	0.4	L/D altitude	38 000 ft
M	0.85		
Mission 4: Los Angeles to London			
payload	30 000 kg	range	5400 nm
w_4	0.4	L/D altitude	38 000 ft
M	0.85		

Table 3: The design mission parameters.

In addition, we also analyze the performance of the aircraft for a 3040 and 5400 nautical mile missions which correspond roughly with the distance from New York to London (JFK to LHR) and Los Angeles to London (LAX to LHR). These two missions were chosen since they are frequently flown long-range routes that this class of aircraft might be assigned. For the optimization problem, these two routes are also assigned a payload of 30 000 kg. For the purposes of optimization, we weight the JFK to LHR and LAX to LHR routes with a 0.4 weights, respectively, while for the extreme maximum range, maximum weight missions we assign an objective weight of 0.1 for each respectively. The rationale is that the performance of the aircraft for these practical missions is more important than the performance in the extreme regions of the payload-range diagram.

5.2 Structural constraints

For the aerostructural problem, we use a series of failure and buckling constraints that are imposed at two points within the design envelope. These are the 2.5g and -1g points illustrated in the V-n diagram shown in Figure 5. For both the failure and buckling constraints we employ a Kreisselmeier-Steinhauser (KS) aggregation technique [18], where we group point-wise constraints from within each element into a small number of global constraints. The KS function can be written as follows:

$$\mathrm{KS} = c_{\max} + \frac{1}{\rho_{KS}} \ln \left[\sum_{i=1}^{N} \exp(\rho_{KS}(c_i - c_{\max})) \right], \tag{20}$$

where c_i are all the point-wise failure or buckling constraints in the aggregation domain, $c_{\max} = \max\{c_1, c_2, \ldots, c_N\}$ is the maximum value of the failure or buckling constraint, and ρ_{KS} is a

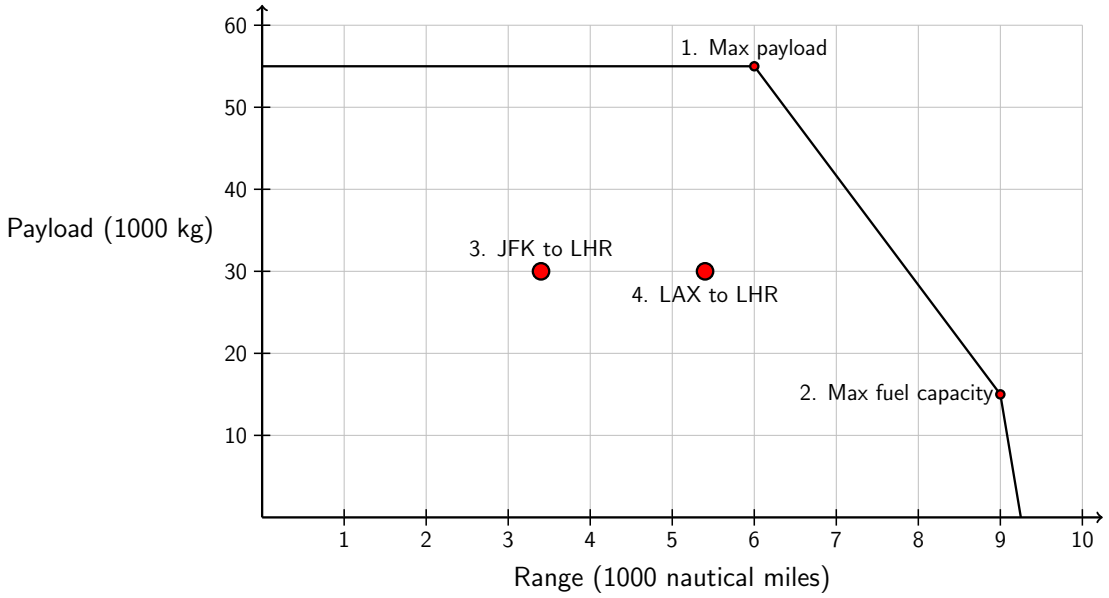

Figure 4: Payload-range diagram for the aircraft

penalty parameter which we take as 80 in all calculations presented here. Since the KS function is conservative, if the failure envelope of the KS function is not violated, then none of the individual element-wise failure functions will be violated. Instead of aggregating all the failure and buckling functions into a single constraint, we group the failure and buckling constraints separately over common structural components. We separate the top and bottom wing skins, respectively and group all spars and ribs into a single KS constraint. Since we do not utilize buckling constraints for the spars and ribs, there are only two KS buckling constraints while there are 3 KS failure constraints for each structural load condition.

5.3 Aerostructural optimization problem

The aerostructural optimization problem can now be summarized as follows: The objective is to minimize a linear combination of the takeoff gross weight and fuel burn over a series of different missions weighted by an imposed objective-weight distribution. Simultaneously, the structural design must satisfy a series of failure and buckling constraints at the two off-design conditions shown in Figure 5 such that the 3 KS failure constraints and 2 KS buckling constraints at each maneuver load are within the admissible failure envelope. In addition, we impose steady-state lift and trim constraints at each of the 6 operating conditions. This is an idealization for the maneuver conditions since, in reality, a steady pull-up condition would require a finite turning radius.

The design variables consist of geometric variables, structural variables, aerodynamic design variables and consistency variables. The aerodynamic design variables consist of the angles of attack at each of the 6 operating conditions. The geometric variables consist of 4 twist variables distributed along the wing span, with a fixed root twist, one span-scaling variable, 5 vertical scaling variables, which modify the thickness to chord ratio, and a single chord scaling variable for the entire wing. Together the span and chord scaling variables admit a series of planforms that are stretched

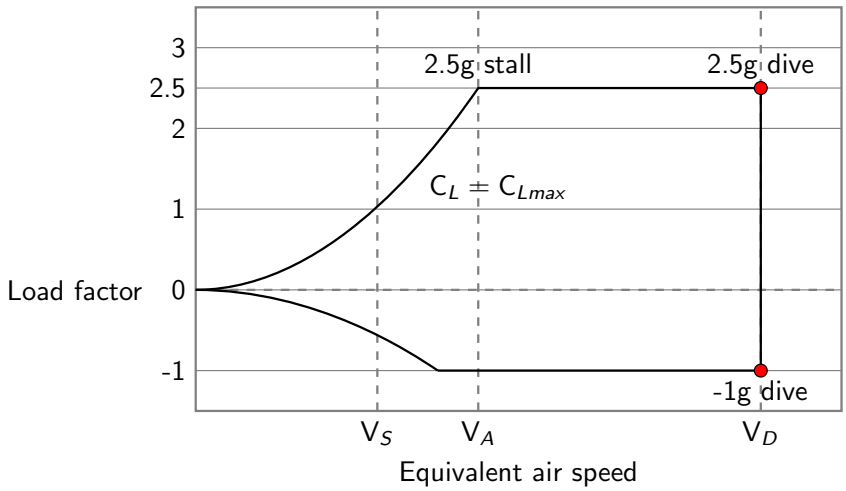

Figure 5: V-n diagram illustrating the points where the structural constraints are imposed.

in the chord-wise and span-wise directions, but share similar geometric features. In addition, we employ 6 tail rotation angle variables in order to trim the aircraft at each flight condition.

For the SP2 and SP3 structural parametrizations, the structural design variables consist of a top stiffener pitch and bottom stiffener pitch variable. Furthermore, this restricts the design such that the stiffener pitch is constant along the entire chord-length of the top and bottom wing skins, respectively. Each panel formed by the leading and trailing edge ribs is assigned the variables shown in Figure 3. Each panel has 2 thickness variables for the skin and stiffener, respectively as well as a panel height. The stiffener base width is fixed based on the stiffener height. For the SP2 parametrization, each material is isotropic and no further information is necessary. For the SP3 parametrization, each material is composite and there are an additional 3 variables that define the ply-fraction for the skin. In this work, we fix the ply-fractions within the stiffeners to a 0^o-ply dominant laminate.

There are several consistency variables that are required in the design problem. First, we add a fuel mass consistency variable for each of the 4 missions. These variables are used in the application of the inertial relief from the fuel loads. They ensure that a fraction of the total fuel load is applied to the wing. In addition, we add an equivalent fuel traction on either the top or bottom skins for each maneuver load. These loads correspond to the surface force per-unit-area exerted by the fuel on the wing. We add a consistency variable for each rib-bay for the entire wing, for each mission. Finally, for the buckling constraints, it is often necessary to have an equivalent panel length, since this information cannot be calculated for each element, we add a length variable for each panel in the wing. We then add a geometric constraint that the physical panel length must match the panel length variable for each component of the wing.

Parameter	Value	Units	Parameter	Value	Units
Aluminum material data					
E	70.0	GPa	ν	0.3	
σ_{YS}	380	MPa	ρ	2780	kg/m^3
Composite material data					
E_1	128	GPa	E_2	11	GPa
G_{12}	4.5	GPa	G_{13}	4.5	GPa
G_{23}	3.2	GPa	ν_{12}	0.25	
X_t	1170	MPa	X_c	1120	MPa
Y_t	40	MPa	Y_c	170	MPa
S	48	MPa	ρ	1522	kg/m^3
Carbon nanotube-based composite material data					
E_1	1200	GPa	E_2	120	GPa
G_{12}	45	GPa	G_{13}	45	GPa
G_{23}	32	GPa	ν_{12}	0.25	
X_t	6000	MPa	X_c	5000	MPa
Y_t	400	MPa	Y_c	1600	MPa
S	500	MPa	ρ	1522	kg/m^3

Table 4: Mechanical properties of the metallic, composite and CNT-based composite used in this study.

The aerostructural optimization problem can be written as follows:

$$
\begin{aligned}
\text{minimize} \quad & \sum_{i=1}^{4} w_i \left(\beta \text{FB} + (1-\beta)\text{TOGW}\right) & & \\
\text{w.r.t.} \quad & \mathbf{x} & & \\
\text{such that} \quad & \text{KS}_{\text{fail}}^{(i)} \leq 1 & & i = 1, \ldots, 6 \\
& \text{KS}_{\text{buckling}}^{(i)} \leq 1 & & i = 1, \ldots, 4 \\
& L^{(i)} = n_{(i)} W^{(i)} & & i = 1, \ldots, 6 \\
& M^{(i)} = 0 & & i = 1, \ldots, 6 \\
& \mathbf{c}(\mathbf{x}) = 0 & & \\
& \mathbf{l} \leq \mathbf{A}\mathbf{x} \leq \mathbf{u} & &
\end{aligned}
\tag{21}
$$

where $\text{KS}_{\text{fail}}^{(i)}$ and $\text{KS}_{\text{buckling}}^{(i)}$ are the KS failure and KS buckling constraints, $L^{(i)} = n_{(i)} W^{(i)}$ and is the lift constraint for each analysis condition, and $n_{(i)}$ is the load factor, $M^{(i)} = 0$ represents the trim condition for each load condition, $\mathbf{c}(\mathbf{x}) = 0$ represents all the consistency constraints and $\mathbf{l} \leq \mathbf{A}\mathbf{x} \leq \mathbf{u}$ represents the adjacency constraints. Note that the consistency constraints are nonlinear but do not depend on the solution of the aerostructural problem directly, therefore their derivatives are inexpensive to evaluate.

Table 4 shows the properties of the materials used in this study including the metallic, composite

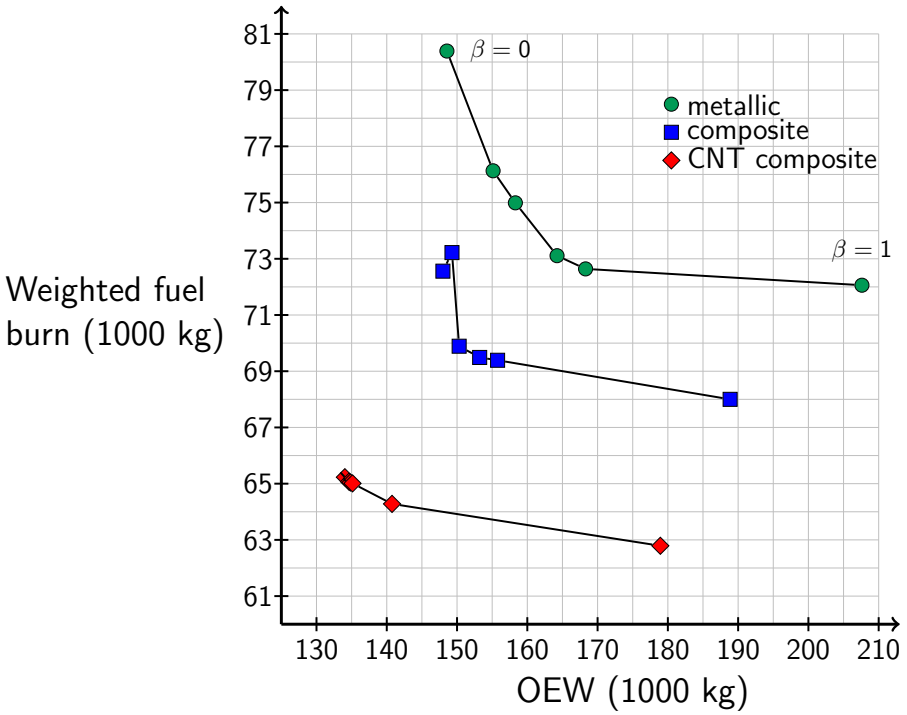

Figure 6: The Pareto front of the weighted sum of the fuel burn vs. OEW of the aircraft.

and CNT-based composite. Note that the CNT-based composite material is based on a tensile modulus of 1.2 TPa and a tensile strength of 6 GPa, while the remaining properties are scaled to match the corresponding composite material data. We apply a 20% knock-down factor to all strength properties to account for material degradation and strength after impact effects.

6 Results and Discussion

In this section, we present the results from a series of optimizations for the metallic, conventional composite and CNT-based composite wings. In order to evaluate the effect of fuel burn and structural weight reduction, we present a series of optimizations that examine the trade-offs between structural weight reduction and fuel burn minimization.

6.1 Aerostructural optimization

Figure 6 shows the Pareto front comparing the optimization results with $\beta = 0$, 0.5, 0.625, 0.75, 0.875, and 1 for the metallic, composite and CNT-based composite wings. Here we plot the Pareto fronts based on the OEW and the weighted sum of the fuel burn from each of the four missions used in the objective function. We plot the OEW rather than TOGW since the TOGW varies depending on the mission, while the OEW is independent of mission. In the context of this study, the Pareto fronts based on OEW or TOGW and weighted fuel burn lie on top of one another since the TOGW can be expressed as a sum of the OEW, the weighted fuel burn, and a constant offset

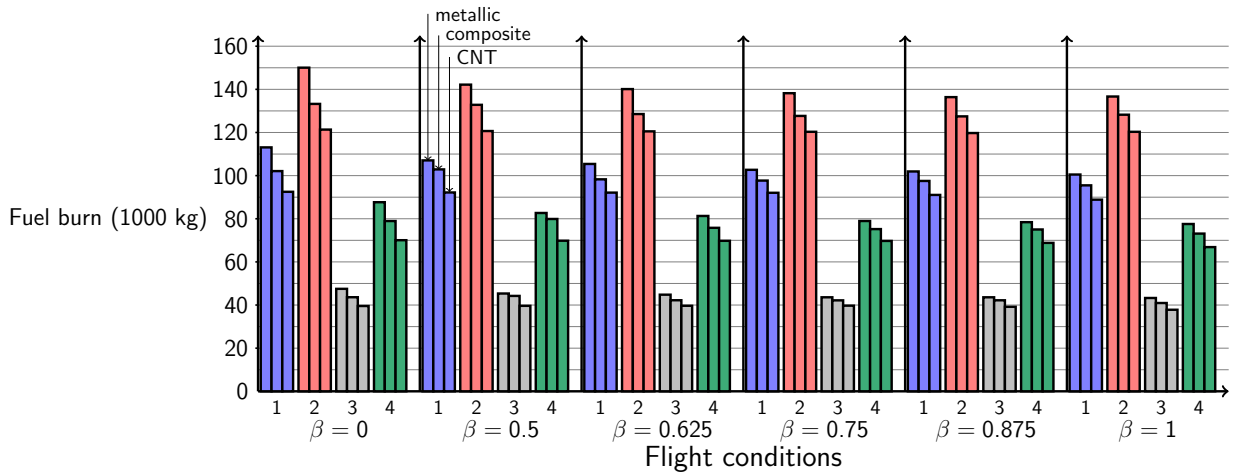

Figure 7: Fuel burn for each of the four missions for the metallic, composite and CNT-based composite wing.

from the reserve mission fuel and payload. Note that the composite wing designed with $\beta = 0.5$ is markedly different from the other composite designs resulting in a non-smooth Pareto front. This discrepancy is due to a premature termination of this optimization which produces a feasible, but not fully optimal design. We are currently investigating the cause of this premature termination.

From Figure 6 it is clear that the use of advanced materials for the wing leads to simultaneous fuel burn and structural weight improvements. As a result, the Pareto fronts for each structural technology shift towards the axis. For the fuel burn objective with $\beta = 1$, the best design for the CNT-based composite wing has a 12% weighted fuel burn advantage over the metallic wing and a 7% weighted fuel burn advantage over the composite wing. However, as β decreases from 1, the shape of the Pareto fronts change significantly. In particular there is a significantly smaller fuel burn penalty for the minimum TOGW designs over the minimum fuel burn designs. This results in Pareto fronts for the composite and CNT-based composite wings that are more compact along the weighted fuel burn axis.

At the other end of the Pareto front, there is a significant increase in OEW between the $\beta = 0.875$ point and the minimum fuel burn designs, while the fuel burn reduction is less than 1% for the metallic case and about 2% for both the composite and CNT-based composite designs, respectively. In each case, the fuel burn reduction between the last two points comes at a significant weight penalty of between 30 000 and 40 000 kg. This result illustrates the importance of correctly modeling the potential drag reduction when considering fuel savings.

Note that the CNT results exhibit a relatively modest 7–11% improvement in the fuel burn given the ten-fold improvement in the material properties of the CNT-based composite. This modest improvement is due to a number of factors. First, only the structural weight of the wing is reduced relative to the other designs. Structural material advances could also be used on other parts of the structure, but assessing the impact of this weight savings is beyond the scope of the current report.

Figure 7 shows the variation of the fuel burn for the four missions analyzed in the design problem

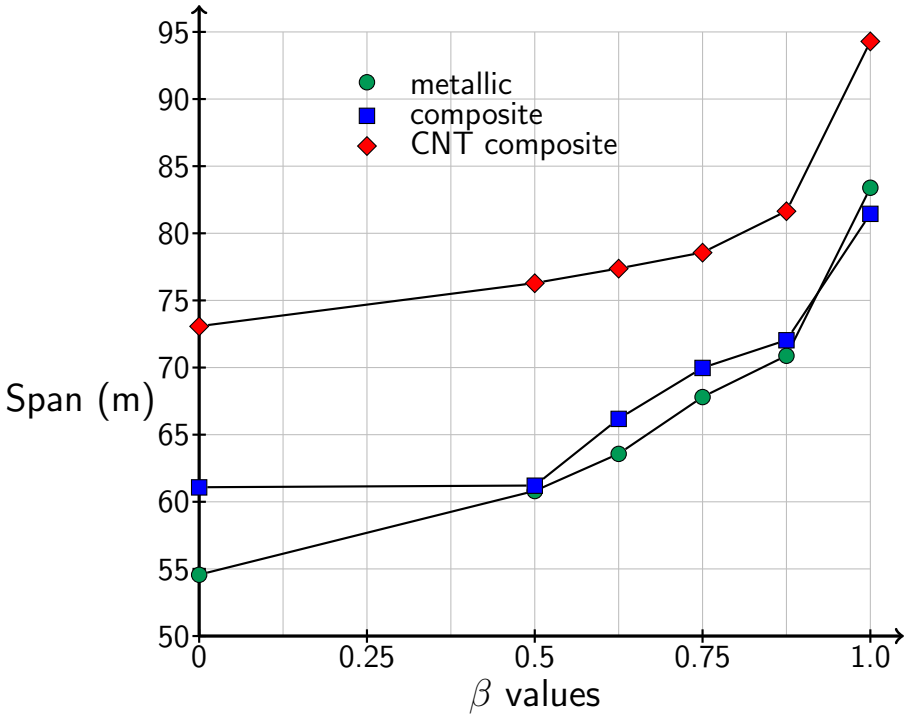

Figure 8: The spans of the metallic and composite wing designs

for the metallic, composite and CNT-based composite wings for $\beta = 0$, 0.5, 0.625, 0.75, 0.875, and 1, respectively. For all missions and all values of β, the fuel burn decreases for increasingly advanced structural technology so that all composite designs burn less fuel than the corresponding metallic designs, and all CNT-based composite designs burn less fuel than the corresponding composite designs. Note that the reduction in fuel burn, in an absolute sense, for increasing structural technology is largest for the $\beta = 0$ designs and smaller for designs with $\beta > 0$. This effect can also be observed in an aggregate sense in the Pareto fronts in Figure 6.

Figure 8 shows the optimal spans for the metallic, composite and CNT-based composite wings. The trend is clear: the wing span increases as fuel burn objective becomes increasingly important. It is reasonable to expect that the spans of the metallic, composite and CNT-based composite wings would be successively larger for a given value of β. However, in the results shown here, the metallic wing span is larger than the composite wing span for $\beta = 1$. This may be due to the structural weight savings achieved by the composite designs which offset the fuel burn savings achieved through a larger wing span, and thus higher L/D ratio.

Figure 8 shows that the wing spans of the final designs, particularly of the composite wings, do not vary as smoothly as expected. This non-smooth behavior may be due in part to the termination of the optimization before the design has reached the full optimality and may also be due to the sensitive nature of the design to the wing span. Typically, the span only increases in the late stages of the design optimization. Presently we are trying to determine the cause of the non-smooth variation of the span and the larger metallic wing span for the fuel burn minimization case.

Figure 9 illustrates the L/D ratios achieved by the final designs at the mid-weight cruise con-

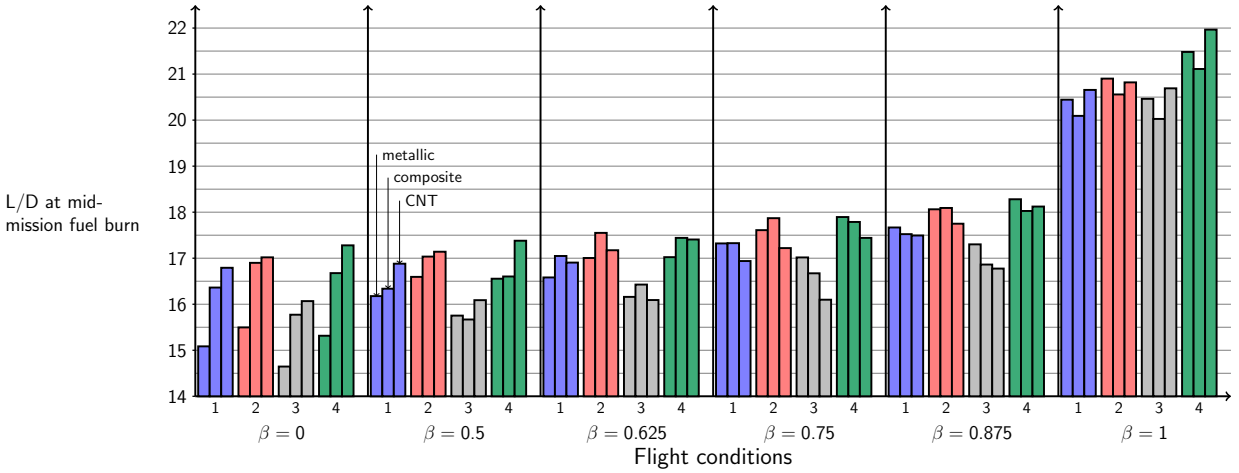

Figure 9: L/D ratio evaluated at the half the mission fuel burn.

ditions for the metallic, composite and CNT-based composite designs. In this case, it would be reasonable to assume that for a given mission, and a given value of β, the optimal L/D ratio should increase with increasing level of technology, however the results presented here do not exhibit this behavior. For the fuel burn minimization results with $\beta = 1$, the composite wings exhibit a lower L/D ratio than the metallic or CNT-based composite designs. In fact, the L/D ratio correlates more closely with the wing span.

Figure 10 shows the planforms of the metallic, composite and CNT-based composite designs for $\beta = 0$, 0.5, 0.75, and 1, respectively. The results show the large span extensions exhibited by the fuel burn optimized designs. In addition, there is relatively little change in the chord scaling variable. As a result, the large span designs also exhibit a large increase in the wetted wing area compared with the baseline QCRM wing.

Figure 11 shows the twist distributions at both the 2.5g maneuver condition and at the mid-weight point of the mission from Los Angeles to London for the metallic, composite and CNT-based composite designs for $\beta = 0$, 0.5, 0.75, and 1, respectively. In most cases, the composite and metallic wings exhibit similar amounts of passive aeroelastic twist. However, the composite and especially CNT-based composite wings are made with a much stiffer material and have much larger wing spans.

Figure 12 shows the lift distributions normalized by dynamic pressure at both the 2.5g maneuver condition and at the mid-weight point of the mission from Los Angeles to London for the metallic, composite and CNT-based composite designs for $\beta = 0$, 0.5, 0.75, and 1, respectively. The designs exhibit varying amounts of load alleviation where, in particular, the lift distribution for the fuel burn designs exhibit a cross-over near the tip. This passive alleviation shifts the load in-board, reducing the bending moment near the wing root.

Figures 13 and 14 show the metallic thickness distribution of the upper and lower wing skins for the optimizations with *beta* = 0, 0.5, 0.75, and 1. For all cases, the thickness is largest at the wing-body join, not the attachment point at the symmetry plane. As expected, the wing panel thickness decreases towards the tip. The distribution of the upper and lower thicknesses are nearly identical. For the design with $\beta = 1$ with the largest wing span, the thickness at the tip increases

slightly. This is due to a combination of inertial relief effects and reduced trim drag by aft-ward motion of the center of gravity.

Figures 15 and 16 show the composite thickness distribution of the upper and lower wing skins for the optimizations with $beta = 0$, 0.5, 0.75, and 1. The thickness of the panels is largest at the side-of-body rather than the symmetry plane, except for the top skin for the $\beta = 1$ case. In the composite cases, there is a non-uniform variation of the thickness on the upper wing skin while the lower wing skin distribution appears to be smooth. We are currently investigating the cause of this variation.

6.2 RANS-based aerodynamic shape optimization

In this section we examine the effects of performing a RANS-based aerodynamic shape optimization on the optimized design obtained from the coupled TACS and TriPan aerostructural design optimization. The goal is to manipulate the airfoil cross sections slightly, improving the overall drag characteristics without comprising the previously optimized structural design. To that end, the planform remains fixed, and only small changes are allowed in the cross-sectional shape through the use of shape design variables. All results in this section are purely aerodynamic and use the undeformed jig shapes from the TACS-Tripan results.

6.2.1 Aerodynamic optimization problem formulation

Without the inclusion of the structural model, the aerodynamic optimization problem formulation is simplified considerably as compared to Equation (21). With a fixed structural model, the Breguet range equation simplifies to the traditional aerodynamic optimization of lift-constrained drag minimization. Our first aerodynamic problem formulation was as follows:

$$\begin{aligned} \text{minimize} \quad & C_D \\ \text{w.r.t.} \quad & \mathbf{x} \\ \text{such that} \quad & C_L = C_L^* \\ & t > t_{\text{init}} \qquad i = 1, \ldots, 425 \end{aligned} \tag{22}$$

where $\mathbf{x}$ is the vector of 192 shape design variables that perturb the surrounding free-form deformation (FFD) box in the y direction. Figure 17 shows the FFD and the allowed motion of the FFD points. C_L^* is the target lift coefficient that is set to 0.5 for all of the following optimizations. In addition, there are 425 airfoil thickness constraints distributed over the entire wing surface and ensure that the thickness of the wing cannot decrease anywhere. However, these constraints still permit changes in the camber distribution at constant local thickness. Any decrease in the depth of the spar box would immediately have a detrimental effect on the structural design and thus must be avoided.

The first optimization we completed was the metallic design for $\beta = 0.75$. A comparison of the initial and optimized lift distributions are given in Figure 18.

Twist variables were not included in the optimization under the assumption that with their absence the optimization formulation would lack sufficient design freedom to significantly alter the original lift distribution. Remarkably, this proved not to be case as shown in Figure 18. The initial lift distribution is roughly similar to the corresponding $\beta = 0.75$ curve in Figure 12. We do not expect these to match however, for two reasons: The current aerodynamic optimization

is performed on the jig shape whereas the aerostructural optimizations account for the deformed shape. Secondly, the effects of the inboard shock are not captured in the panel method simulation and this results in a more inboard-shifted load distribution than predicted by the TriPan simulation.

The aerodynamic optimization nearly recovers a perfect elliptical lift distribution. This large change in lift distribution is even more unexpected when it is considered that both the initial and optimized configurations are twisted by more than 14° along the span-wise direction. This result highlights the capability of the RANS-based optimization framework: Even with a restrictive set of design variables the optimization has produced a shock-free wing *and* elliptical lift distribution. It is therefore clear that the new optimized aerodynamic design would require substantial changes to the structural design to ensure that both the failure and buckling constraints can be met.

In an effort to prevent significant changes to the initial lift distribution, we modified the design formulation to include a root bending moment constraint. This constraint is designed to act as a very simple surrogate for the structure design by enforcing that the root bending moment of the optimized design can be no larger than the initial bending moment. While there is no guarantee that structural failure constraints will still be satisfied after the aerodynamic-only optimization, we expect that the bending moment constraint surrogate will limit the amount of infeasibility in the structural constraints. The modified aerodynamic optimization problem is given below:

$$\begin{aligned} \text{minimize} \quad & C_D \\ \text{w.r.t.} \quad & \mathbf{x} \\ \text{such that} \quad & C_L = C_L^* \\ & t > t_{\text{init}} \qquad i = 1, \ldots, 425 \\ & C_{M_x} < C_{M_{x\,\text{init}}} \end{aligned} \tag{23}$$

The initial value for the C_{M_x} constraint is obtained by first performing a single flow solution at C_L^*.

6.2.2 Metallic optimization results

Using the bending-moment constrained formulation, aerodynamic optimizations were completed for each of the six metallic wing designs.

Figure 19 shows the surface mesh distribution, aerodynamic solution, and shock surface visualization (isosurface where $(\mathbf{U}/a) \cdot (\nabla P/\|\nabla P\|) = 1.0$, where U is the velocity vector a is the speed of sound and P is the pressure) for the metallic $\beta = 0.75$ design before optimization. The strong shock on the inboard section of the wing is due to higher nose-up twist values near the wing root as compared to the remainder of the wing. The grids and flow solutions for the other initial designs show a similar shock pattern.

The aerodynamic mesh contains approximately 700 000 hexahedreal cells and optimizations are performed using 64 processors. Optimizations required between 70 and 105 iterations and approximately 7 hours of wall time to reduce the optimality to 5×10^{-5}.

The evolution of the drag coefficient for each of the six optimizations is given in Figure 20. In all cases, significant drag reduction is achieved, primarily due to the elimination of the shock on the inboard section of the wing. The higher relative and absolute drag reductions on the lower β values is due to the higher initial shock strength on these designs. A comparison of the initial and optimized drag values (given in drag counts) is given in Table 5.

Table 5: Initial and optimized drag values in drag counts (ct).

β	Initial Value (ct)	Optimized Value (ct)	Delta (ct)	% Change
0.000	243.69	202.92	-40.77	-16.7
0.500	223.58	184.89	-38.69	-17.3
0.625	212.10	177.65	-34.45	-16.2
0.750	196.02	169.63	-26.39	-13.5
0.875	192.00	164.46	-27.54	-14.3
1.000	169.70	152.16	-17.54	-10.3

Lift distributions for each of six optimizations are given in Figure 21. The effect of the bending moment constraint is now clear. In all cases the highly inboard loaded lift distributions have been smoothed while retaining the same root bending moment. The optimized lift distributions indicate that a nearly linear lift distribution is optimal for aerodynamic optimizations largely governed by the fixed bending moment constraint. Note that even though each of the six designs have different spans, the *shape* of the initial and optimized distributions are very similar.

It is also instructive to compare the drag values from the two $\beta = 0.75$ optimizations; one with a bending moment (C_{M_x}) constraint and one without. The constrained optimization resulted in 169.63 drag counts while the unconstrained optimization (with a nearly elliptical lift distribution) yielded 146.90 counts or approximately 14%. Since both solutions have no significant regions of separated flow and are almost entirely shock free at the optimized design point, we can conclude that this drag differential is due primarily to the different lift distributions. This drag differential would represent approximately 10% of the total drag on a complete 777-like airframe.

Finally we examine a three dimensional view of the C_p contours on the optimized designs shown in Figure 22. In all cases, the initial inboard shock has been completely eliminated and the smooth, parallel C_p isobars indicate a smooth pressure recovery right up to the trailing edge.

A two dimensional slice of the wing at the parametric half-semi-span location shown in Figure 23 shows very precisely the power of the aerodynamic shape optimization to eliminate shocks and reduce the resulting wave drag. It is particularly interesting to see just how little shape modification is necessary to achieve these effects. Slight thickness increases and redistribution of camber is enough to have a significant effect on the overall drag. Recall the twist distributions are fixed and only thickness increases are allowed. Even with this very restrictive search space, all optimizations yield significant aerodynamic improvements within the supplied constraints.

7 Conclusions

While some results raise new questions that require further investigation, the following conclusions can be drawn from the results obtained so far:

1. The QCRM wing developed for this study seems suitable to evaluate the material trade-offs for transonic transport wings.

2. Conventional composite wings exhibit a fuel burn that is 4–8% lower than metallic wings.

3. CNT composite wings, in spite of an elastic modulus and strength that is about ten times higher than conventional composites, exhibits a relatively modest improvement in fuel burn

(7–11%). This is in part because the structural weight of components other than the wing were assumed to be constant, and in part because many of the CNT structural thicknesses converged to the lower bound.

4. The computation of fuel burn versus empty weight Pareto fronts provided valuable information in terms of the magnitude of the trade-offs involved for the various materials. The span of the Pareto fronts in both axes decreased with better materials, as there the trade-off between fuel-burn and weight became less dramatic.

5. CNT-based composite optimal wings have a span that is 13–30% larger than their metallic and conventional composite counterparts.

6. At the optimum, the fuel burn and TOGW are very insensitive to the span. This needs to be investigated further.

7. Using RANS-based aerodynamic shape optimization, it is possible to further reduce the drag by up to 14%, with no structural weight penalty.

References

[1] Mader, C. A., Martins, J. R. R. A., Alonso, J. J., and van der Weide, E., "ADjoint: An Approach for the Rapid Development of Discrete Adjoint Solvers," *AIAA Journal*, Vol. 46, No. 4, April 2008, pp. 863–873. doi:10.2514/1.29123.

[2] Lyu, Z., Kenway, G. K., Paige, C., and Martins, J. R. R. A., "Automatic Differentiation Adjoint of the Reynolds-Averaged Navier–Stokes Equations with a Turbulence Model," *21st AIAA Computational Fluid Dynamics Conference*, San Diego, CA, Jul 2013. doi:10.2514/6.2013-2581.

[3] Kennedy, G. J. and Martins, J. R. R. A., "Parallel solution methods for aerostructural analysis and design optimization," *Proceedings of the 13th AIAA/ISSMO Multidisciplinary Analysis Optimization Conference*, Fort Worth, TX, September 2010, AIAA 2010-9308.

[4] Kenway, G. K. W., Kennedy, G. J., and Martins, J. R. R. A., "Scalable Parallel Approach for High-Fidelity Steady-State Aeroelastic Analysis and Derivative Computations," *AIAA Journal*, 2014. doi:10.2514/1.J052255, (In press).

[5] Katz, J. and Plotkin, A., *Low–Speed Aerodynamics*, McGraw–Hill Inc., 1991.

[6] Balay, S., Gropp, W. D., McInnes, L. C., and Smith, B. F., "Efficient Management of Parallelism in Object Oriented Numerical Software Libraries," *Modern Software Tools in Scientific Computing*, edited by E. Arge, A. M. Bruaset, and H. P. Langtangen, Birkhäuser Press, 1997, pp. 163–202.

[7] Kenway, G. K. W. and Martins, J. R. R. A., "Multi-Point High-Fidelity Aerostructural Optimization of a Transport Aircraft Configuration," *Journal of Aircraft*, Vol. 51, No. 1, 2014, pp. 144–160. doi:10.2514/1.C032150.

[8] Hopkins, E. J., "Charts for predicting turbulent skin friction from the van Driest method (II)," Tech. Rep. TN D-6945, NASA, October 1972.

[9] Wakayama, S. and Kroo, I., "Subsonic wing planform design using multidisciplinary optimization," *Journal of Aircraft*, Vol. 32, No. 4, 1995, pp. 746–753. doi:10.2514/3.46786.

[10] Brown, S., "Displacement extrapolation for CFD+CSM aeroelastic analysis," *38th Structures, Structural Dynamics, and Materials Conference*, April 1997. doi:10.2514/6.1997-1090, AIAA97-1090.

[11] Saad, Y. and Schultz, M. H., "GMRES: A generalized minimal residual algorithm for solving nonsymmetric linear systems," *SIAM Journal on Scientific and Statistical Computing*, Vol. 7, No. 3, 1986, pp. 856–869. doi:10.1137/0907058.

[12] Martins, J. R. R. A. and Hwang, J. T., "Review and Unification of Methods for Computing Derivatives of Multidisciplinary Computational Models," *AIAA Journal*, Vol. 51, No. 11, 2013, pp. 2582–2599. doi:10.2514/1.J052184.

[13] Martins, J. R. R. A., Alonso, J. J., and Reuther, J. J., "A Coupled-Adjoint Sensitivity Analysis Method for High-Fidelity Aero-Structural Design," *Optimization and Engineering*, Vol. 6, No. 1, March 2005, pp. 33–62. doi:10.1023/B:OPTE.0000048536.47956.62.

[14] Martins, J. R. R. A., Alonso, J. J., and Reuther, J. J., "High-Fidelity Aerostructural Design Optimization of a Supersonic Business Jet," *Journal of Aircraft*, Vol. 41, No. 3, 2004, pp. 523–530. doi:10.2514/1.11478.

[15] Vassberg, J. C., "A Unified Baseline Grid about the Common Research Model Wing-Body for the Fifth AIAA CFD Drag Prediction Workshop," *29th Applied Aerodynamics Conference*, Honolulu, Hawaii, June 2011. doi:10.2514/6.2011-3508, AIAA 2011-3508.

[16] Stroud, W. J. and Agranoff, N., "Minimum mass design of filamentary composite panels under combined loads: Design procedure based on simplified buckling equations," Tech. rep., NASA Langley Research Center, Hampton, VA 23665, October 1976.

[17] Jones, R. M., *Mechanics of Composite Materials*, Technomic Publishing Co., 1996.

[18] Poon, N. M. K. and Martins, J. R. R. A., "An Adaptive Approach to Constraint Aggregation Using Adjoint Sensitivity Analysis," *Structural and Multidisciplinary Optimization*, Vol. 34, No. 1, 2007, pp. 61–73. doi:10.1007/s00158-006-0061-7.

[19] Lyu, Z., Kenway, G. K. W., and Martins, J. R. R. A., "RANS-based Aerodynamic Shape Optimization Investigations of the Common Research Model Wing," *Proceedings of the AIAA Science and Technology Forum and Exposition (SciTech)*, National Harbor, MD, January 2014. doi:10.2514/6.2014-0567, AIAA-2014-0567.

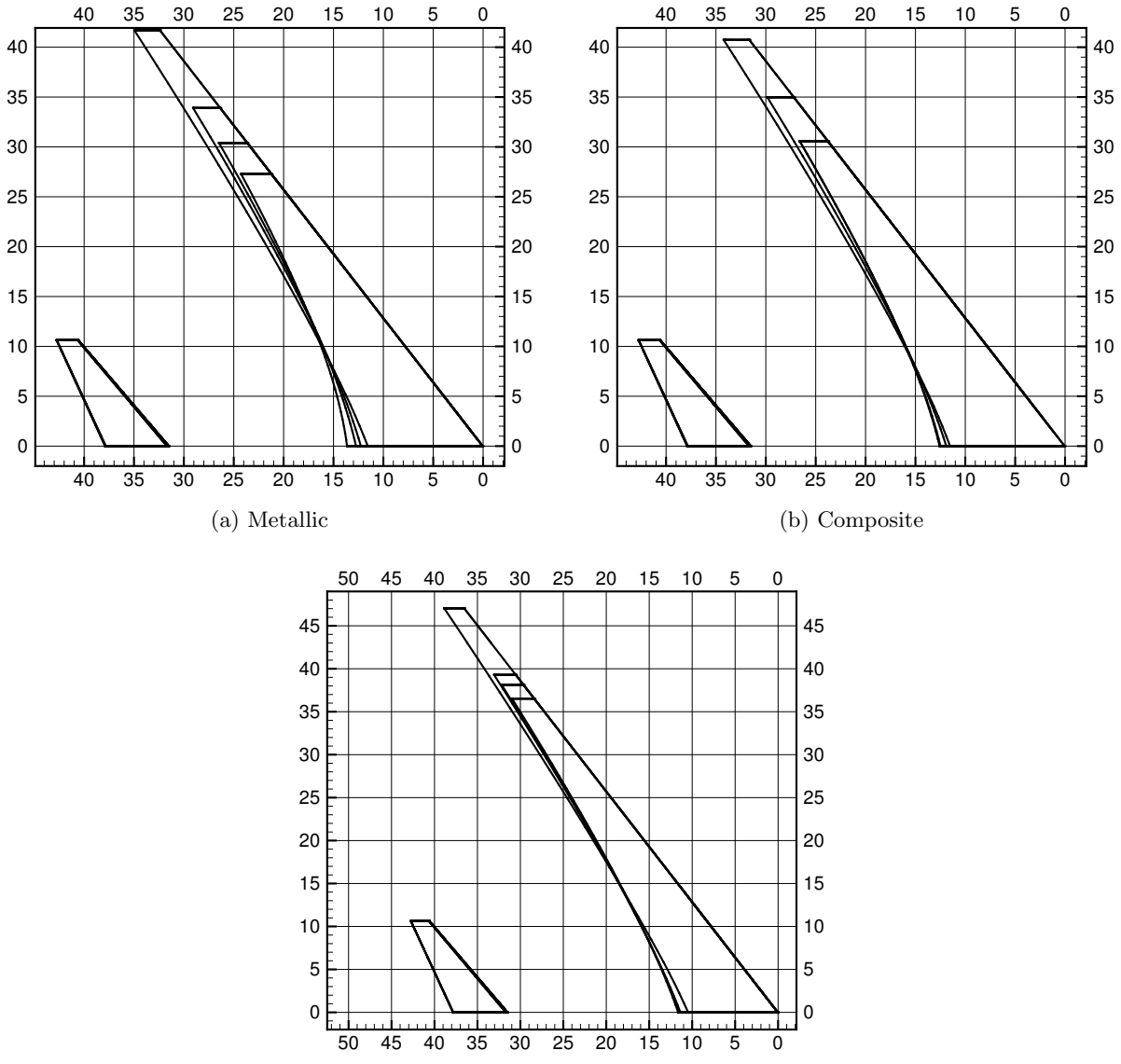

(a) Metallic

(b) Composite

(c) CNT

Figure 10: The planforms of the metallic, composite and CNT-based composite wings.

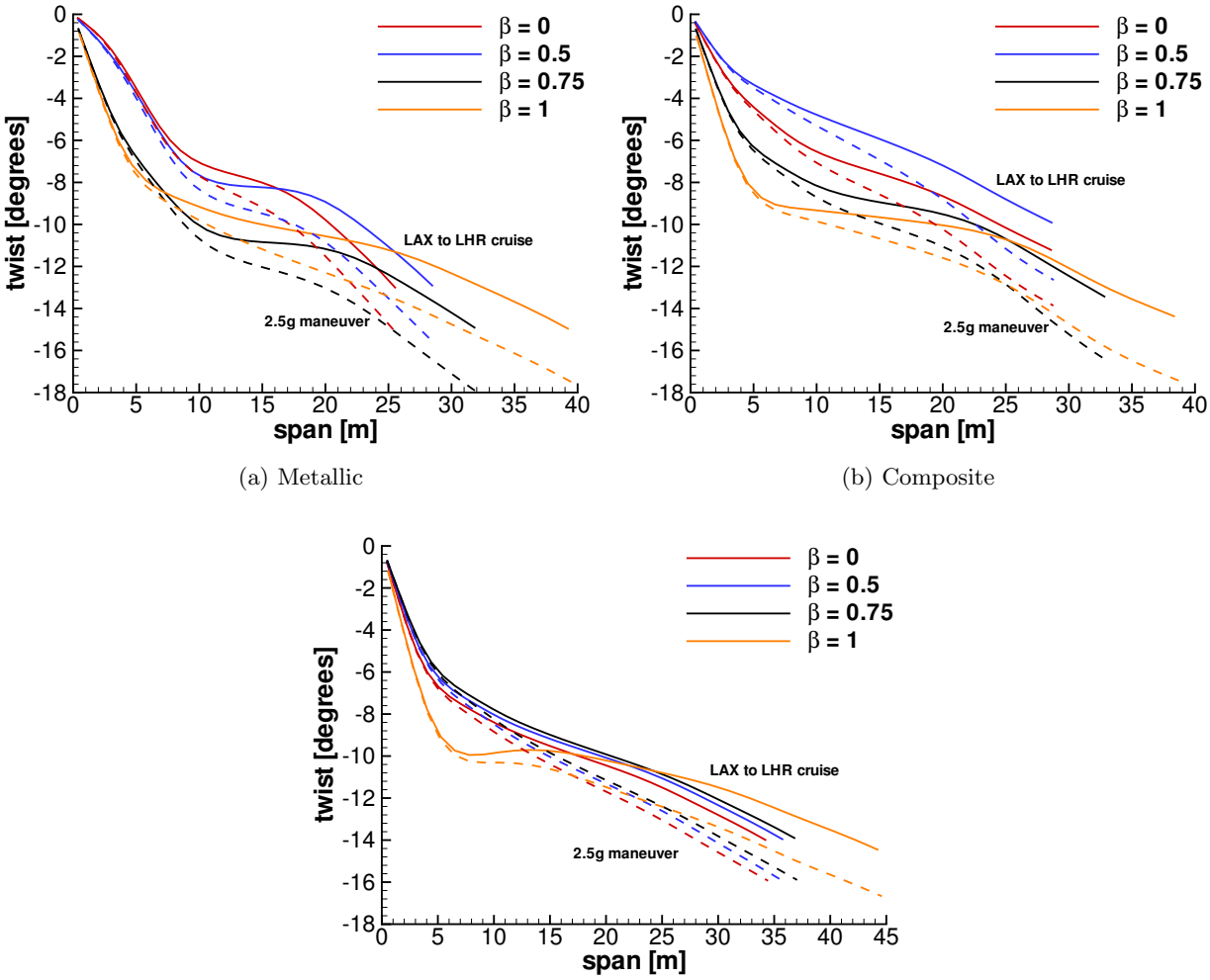

(a) Metallic

(b) Composite

(c) CNT

Figure 11: Twist distributions for the metallic, composite and CNT-based composite wings at both the 2.5g maneuver condition and the cruise condition from LAX to LHR.

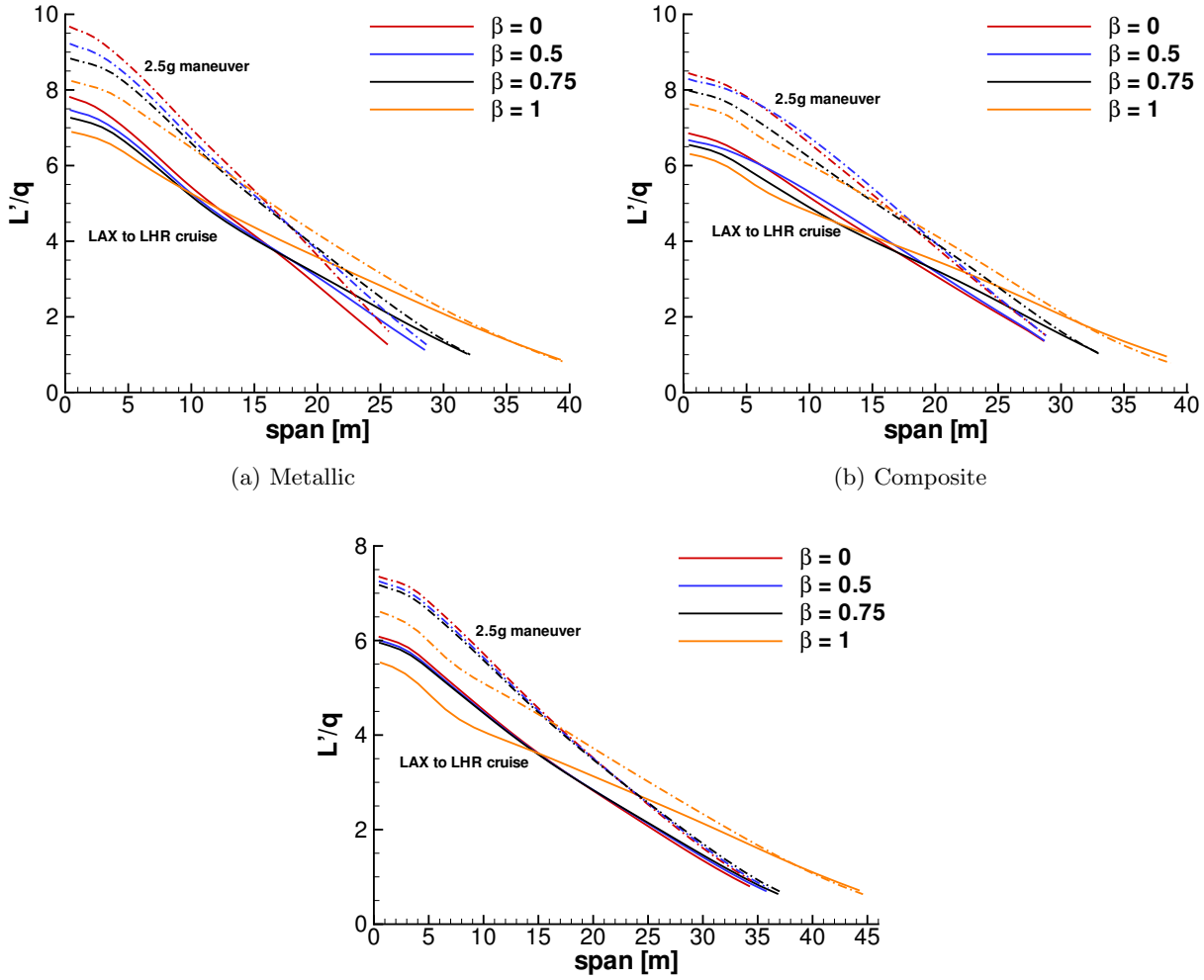

(a) Metallic

(b) Composite

(c) CNT

Figure 12: Lift distributions for the metallic, composite and CNT-based composite wings for both the 2.5g maneuver condition and the cruise condition from LAX to LHR.

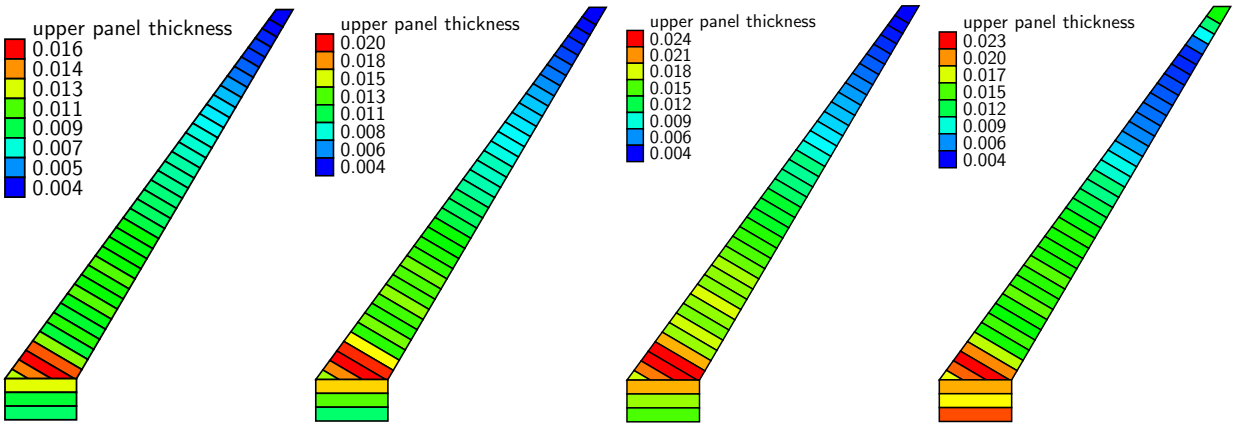

(a) $\beta = 0$ (b) $\beta = 0.5$ (c) $\beta = 0.75$ (d) $\beta = 1$

Figure 13: The lower panel thickness distributions for the metallic wings in meters.

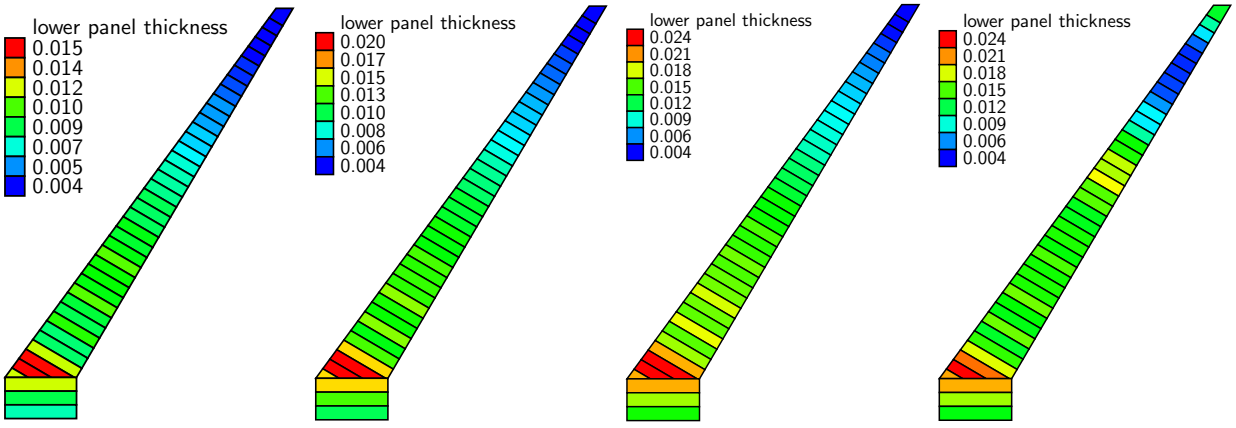

(a) $\beta = 0$ (b) $\beta = 0.5$ (c) $\beta = 0.75$ (d) $\beta = 1$

Figure 14: The lower panel thickness distributions for the metallic wings in meters.

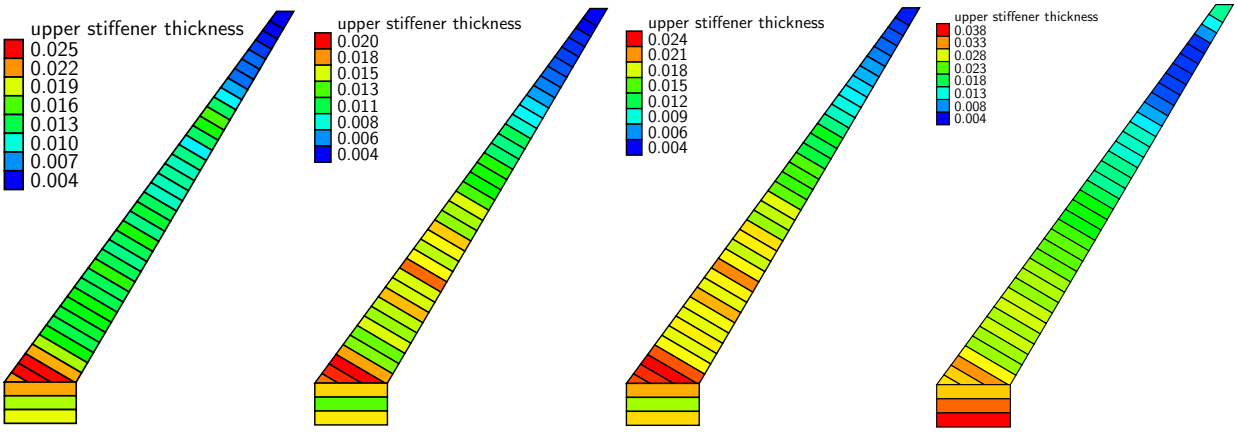

(a) $\beta = 0$ (b) $\beta = 0.5$ (c) $\beta = 0.75$ (d) $\beta = 1$

Figure 15: The lower panel thickness distributions for the composite wings in meters.

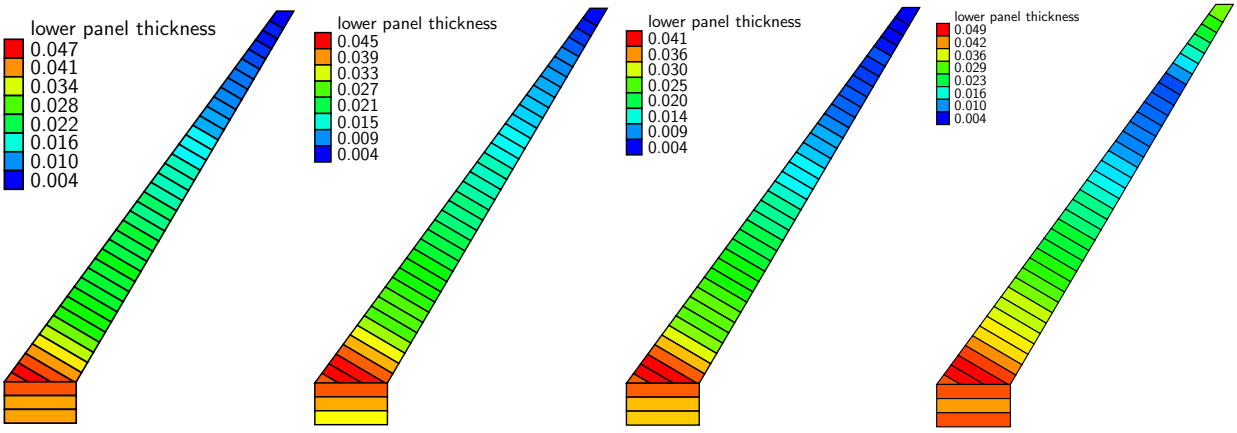

(a) $\beta = 0$ (b) $\beta = 0.5$ (c) $\beta = 0.75$ (d) $\beta = 1$

Figure 16: The lower panel thickness distributions for the composite wings in meters.

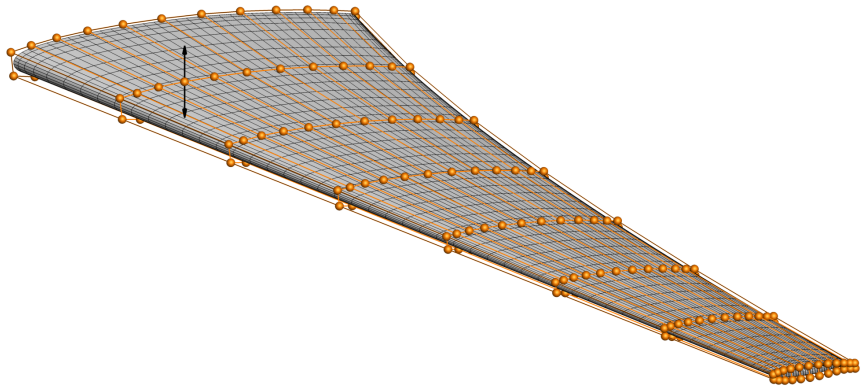

Figure 17: Free form deformation (FFD) volume with 192 control points and the initial CFD surface.

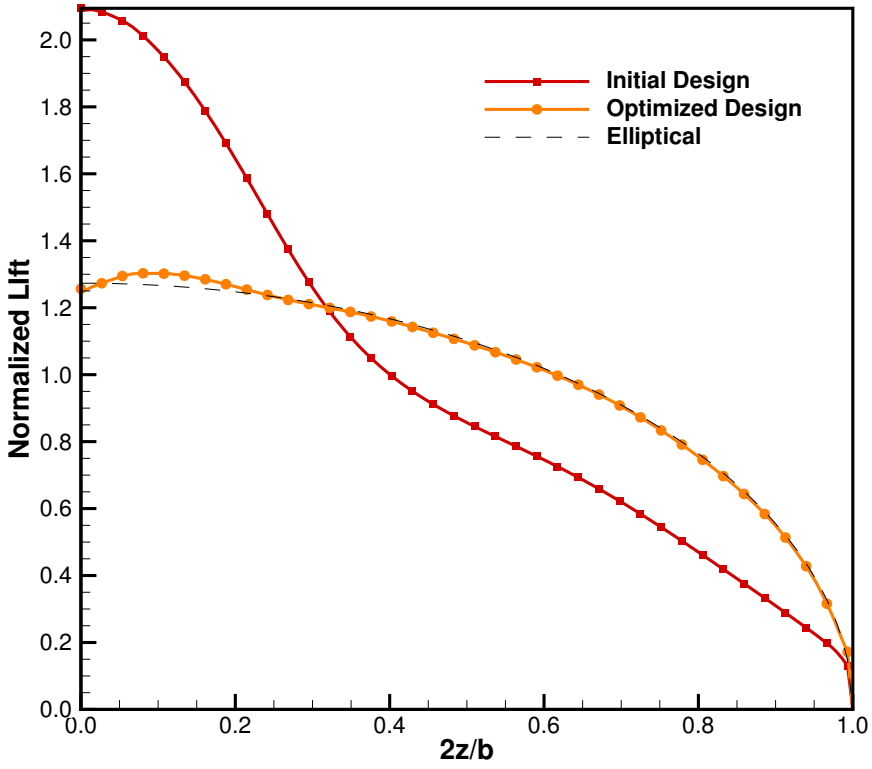

Figure 18: Lift-constrained drag minimization of metallic design ($\beta = 0.75$) with 192 shape design variables.

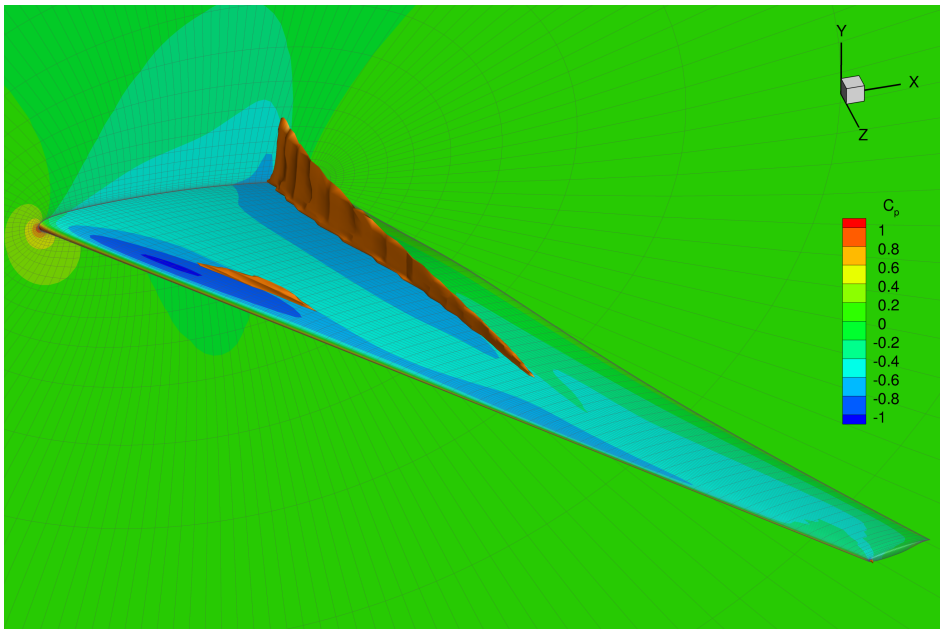

Figure 19: Initial design for metallic $\beta = 0.75$.

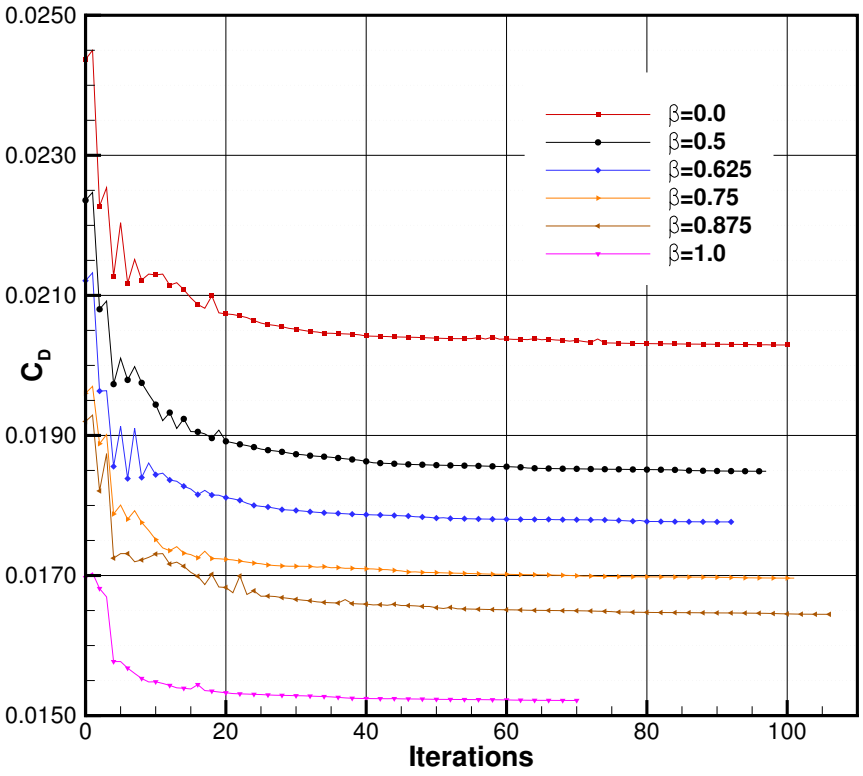

Figure 20: Change in drag coefficient during optimization for each design.

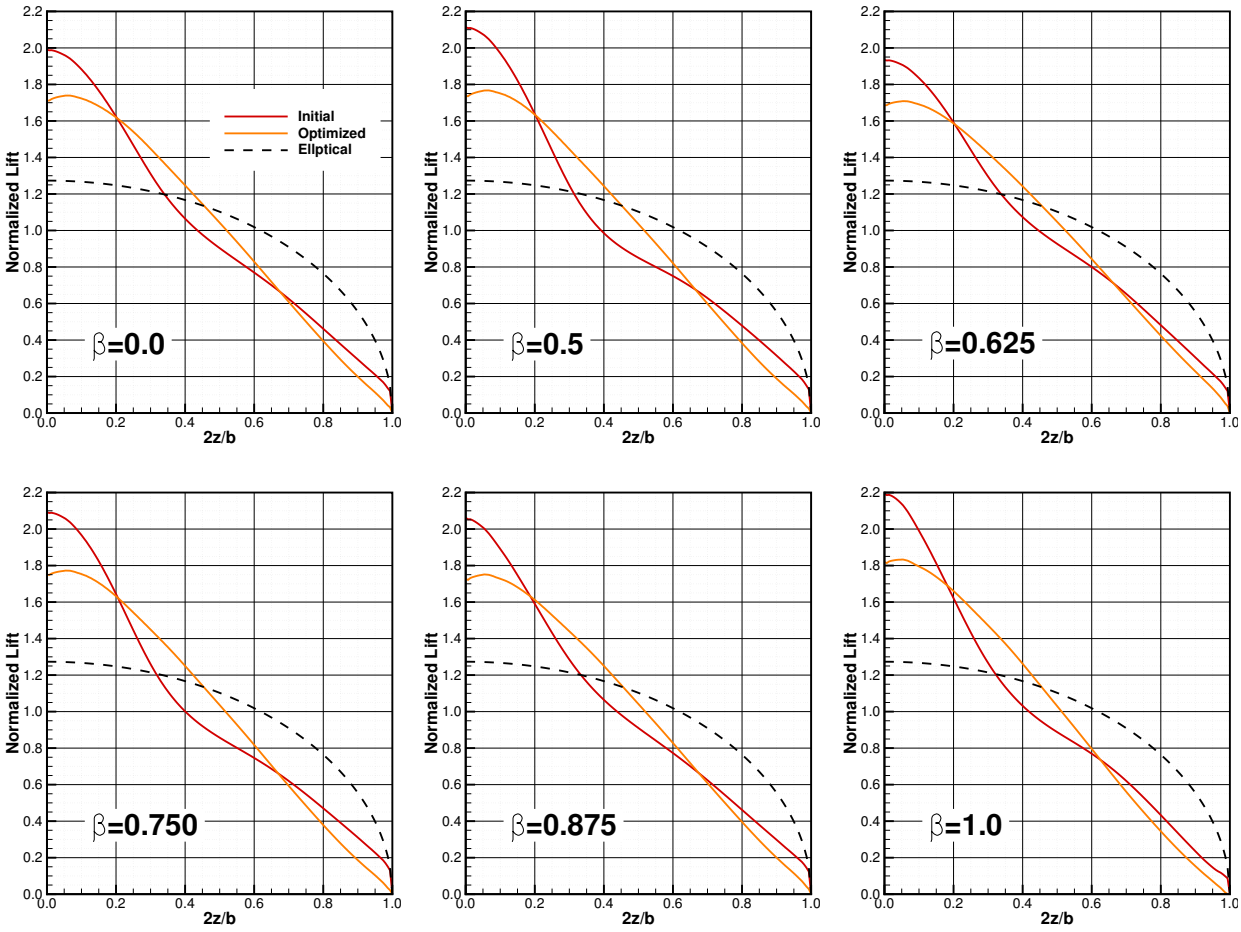

Figure 21: Comparison of initial and optimized lift distributions for all designs.

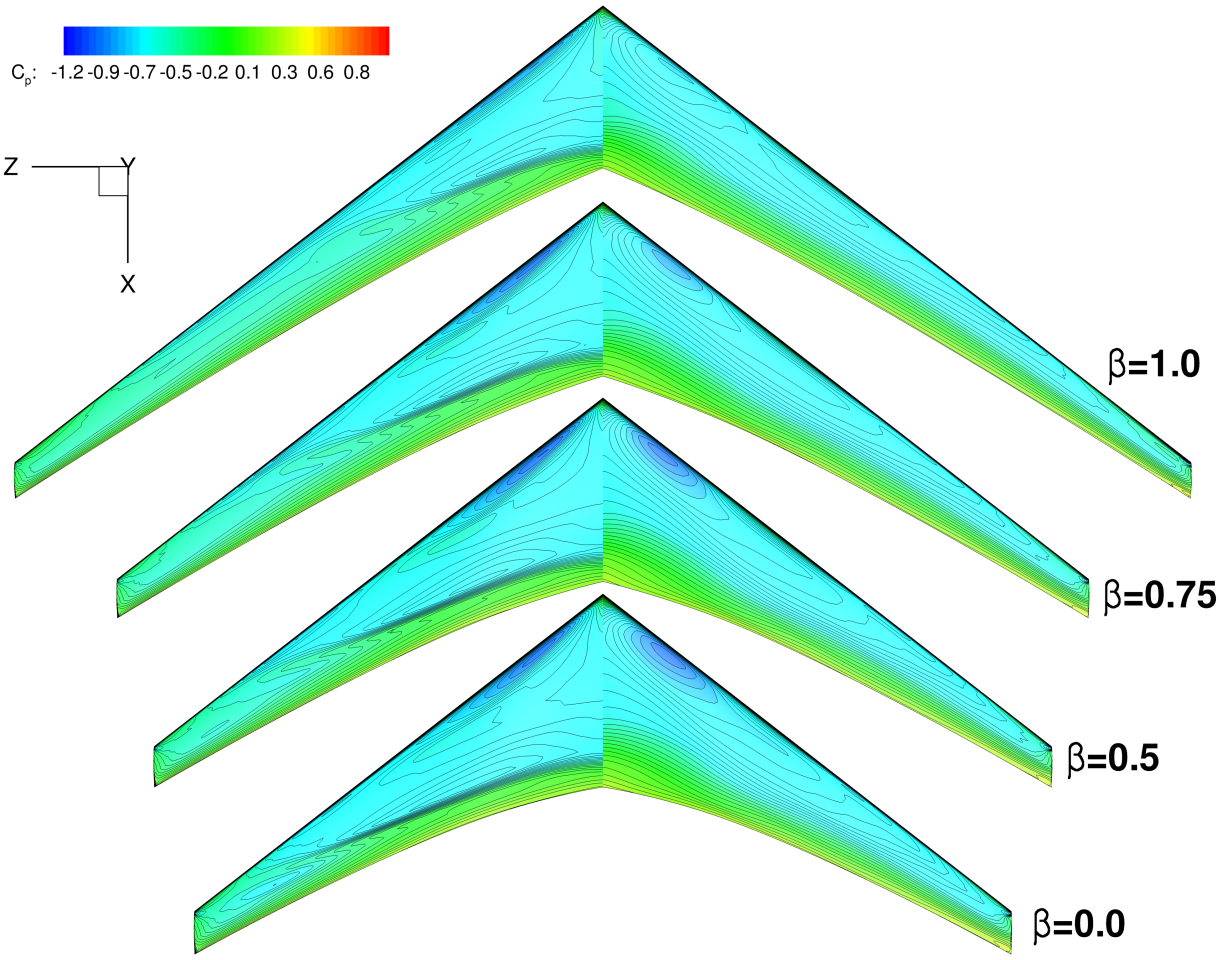

Figure 22: C_p contours for initial (left) and optimized (right) designs.

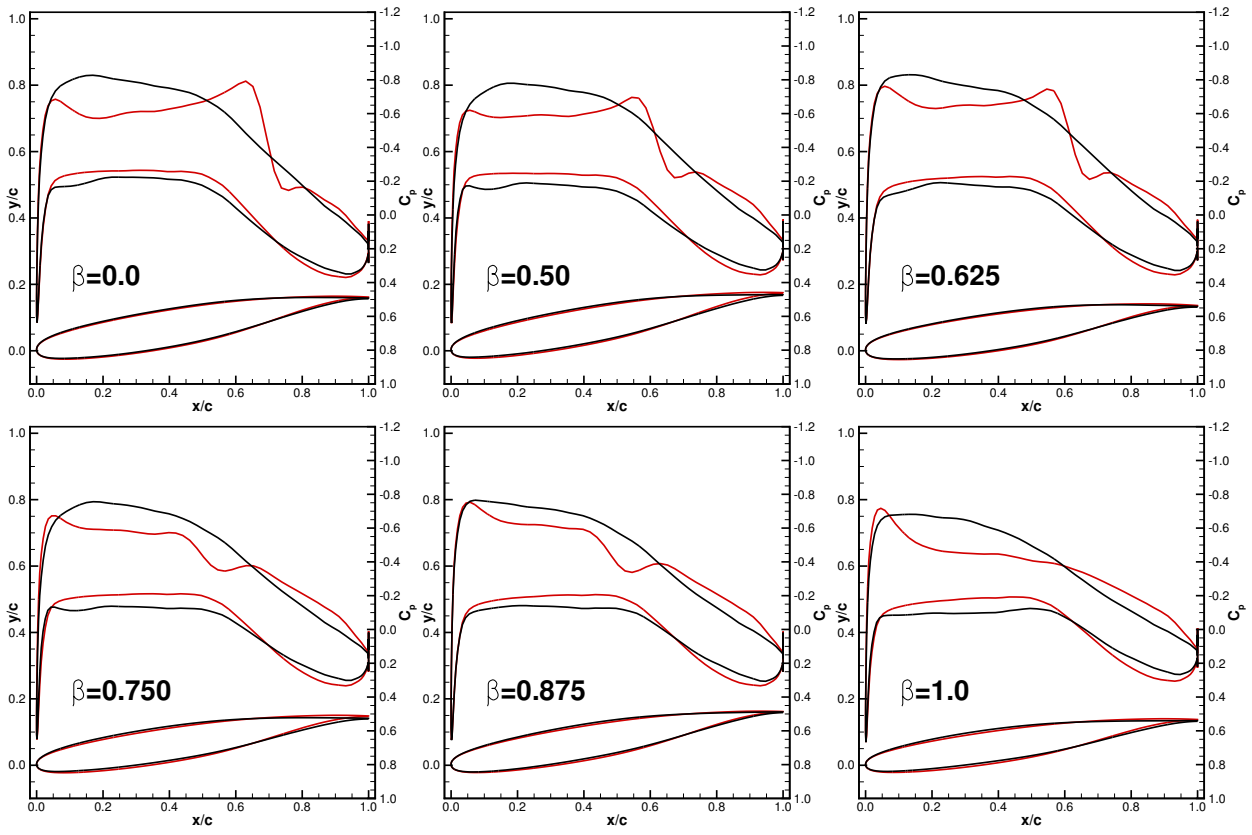

Figure 23: Comparison of cross section and C_p distribution at $2z/b = 0.5$. Red is initial design, black is optimized design.

REPORT DOCUMENTATION PAGE

Form Approved
OMB No. 0704-0188

1. REPORT DATE *(DD-MM-YYYY)*	2. REPORT TYPE	3. DATES COVERED *(From - To)*
01-03-2014	Contractor Report	

4. TITLE AND SUBTITLE

A Comparison of Metallic, Composite and Nanocomposite Optimal Transonic Transport Wings

5a. CONTRACT NUMBER

5b. GRANT NUMBER

NNX11AI19A

5c. PROGRAM ELEMENT NUMBER

6. AUTHOR(S)

Kennedy, Graeme J.; Kenway, Gaetan K. W.; Martins, Joaquim R. R.

5d. PROJECT NUMBER

5e. TASK NUMBER

5f. WORK UNIT NUMBER

432938.11.01.07.43.40.08

7. PERFORMING ORGANIZATION NAME(S) AND ADDRESS(ES)

NASA Langley Research Center
Hampton, Virginia 23681

8. PERFORMING ORGANIZATION REPORT NUMBER

9. SPONSORING/MONITORING AGENCY NAME(S) AND ADDRESS(ES)

National Aeronautics and Space Administration
Washington, DC 20546-0001

10. SPONSOR/MONITOR'S ACRONYM(S)

NASA

11. SPONSOR/MONITOR'S REPORT NUMBER(S)

NASA/CR-2014-218185

12. DISTRIBUTION/AVAILABILITY STATEMENT

Unclassified - Unlimited
Subject Category 02
Availability: NASA CASI (443) 757-5802

13. SUPPLEMENTARY NOTES

Langley Technical Monitor: Karen M. Taminger

14. ABSTRACT

Current and future composite material technologies have the potential to greatly improve the performance of large transport aircraft. However, the coupling between aerodynamics and structures makes it challenging to design optimal flexible wings, and the transonic flight regime requires high fidelity computational models. We address these challenges by solving a series of high-fidelity aerostructural optimization problems that explore the design space for the wing of a large transport aircraft. We consider three different materials: aluminum, carbon-fiber reinforced composites and an hypothetical composite based on carbon nanotubes. The design variables consist of both aerodynamic shape (including span), structural sizing, and ply angle fractions in the case of composites. Pareto fronts with respect to structural weight and fuel burn are generated. The wing performance in each case is optimized subject to stress and buckling constraints. We found that composite wings consistently resulted in lower fuel burn and lower structural weight, and that the carbon nanotube composite did not yield the increase in performance one would expect from a material with such outstanding properties. This indicates that there might be diminishing returns when it comes to the application of advanced materials to wing design, requiring further investigation.

15. SUBJECT TERMS

Aerodynamics; Composite materials; Metal matrix composites; Transonic flight; Wings

16. SECURITY CLASSIFICATION OF:			17. LIMITATION OF ABSTRACT	18. NUMBER OF PAGES	19a. NAME OF RESPONSIBLE PERSON
a. REPORT	b. ABSTRACT	c. THIS PAGE			STI Help Desk (email: help@sti.nasa.gov)
					19b. TELEPHONE NUMBER *(Include area code)*
U	U	U	UU	41	(443) 757-5802